Photoemission Spectra Calculation of Boron-Doped Diamond Using Quantum Monte Carlo Method

Jifeng Yu

DOCTOR OF PHILOSOPHY

Student No. 20041304

Department of Materials Structure Science

School of High Energy Accelerator Science

The Graduate University for Advanced Studies

2007 (School Year)

Contents

Chapter 1: Introduction

In solid state physics, the electron-phonon (*e*-ph) coupling is quite ubiquitous, and plays a central role in influencing the electronic conductivity, the optical property and the electronic band structure, even determining a material to be a semiconductor, metal or superconductor. Recently, the remarkable discovery of superconductivity (SC) in boron-doped diamond (BDD) [1] fostered renewed interests in the *e*-ph discussion, because most investigations support that the pairing is driven by the phonon exchange mechanism [2-6], though with the unsolved controversy about the very nature of this exchange mechanism. One side deems that the function of the doped boron atoms is to shift the Fermi level and supply holes, thus enabling the phonon-hole interaction (because of loss electrons by doping boron) to soften the optical phonons [2-4]; The other insists that the boron atoms introduce localized vibrational modes which can strongly interact with electrons at around the Fermi surface [5, 6]. There is also a suggestion from F. Giustino *et al.* [7] that the SC should be explained by taking into account the finite-wave-vector components ($q > 2k_F$, where q is the phonon wave vector, and $2k_F$ is the average Fermi surface diameter,) of the vibrational modes introduced by boron, except for the significant contribution of the wave vectors around zone-center ($q < 2k_F$) which have been investigated by the above two parties. Whatsoever, the dopant boron has dominant effect on the SC in this material. Correspondingly, the BDD has become one of the most vigorously studied materials by both experiment and theory. Thereinto, the x-ray absorption (XAS) and the

emission (XES) spectroscopy [8, 9], the photoemission spectroscopy (PES) [10, 11] are two typical experimental methods. While the density functional (DF) [2, 4-7, 14], the coherent potential approximation (CPA) [12, 13], and purely electronic mechanism studies [15] compose the majority of theoretical researches.

As a brief review, firstly we present the pristine diamond band structure in Fig. 1 by the local density functional approximation (LDA) calculation [16]. A big gap (about 5.5eV [19]) is clearly seen and the Fermi level lies at the top of valence band. In fact the material is a wide gap insulator. Being lightly doped by boron, it presents *p*-type character with an activation energy gap of about 0.37eV [20]. On increasing the doping percentage to a certain level, the material undergoes the semiconductor-metal transition. Fig. 2 shows a heavily doped diamond band structure from LDA calculation [2] with (dashed lines) and without (solid) a frozen phonon. The Fermi level deeply enters the valence band, and the sample is obviously a metal.

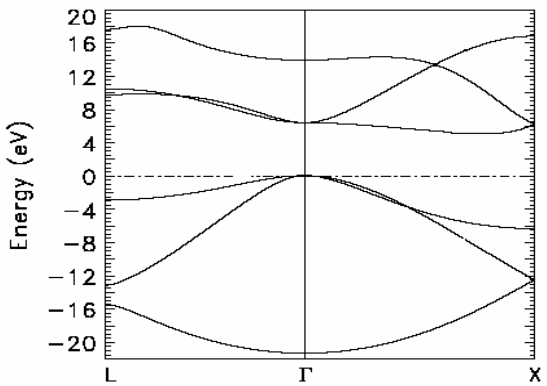

Fig. 1. The band structure of the pure diamond along symmetry directions L and X by LDA calculation. The dashed line at zero is the position of the Fermi level. [16]

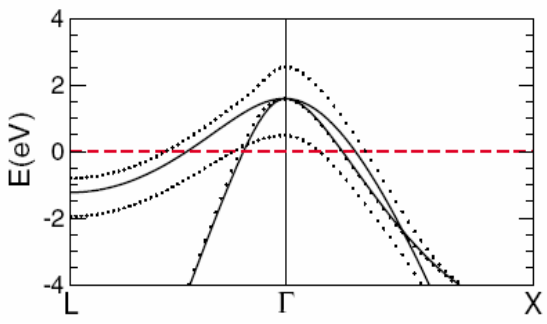

Fig. 2. The band structure of BDD without (dashed lines) and with (solid) a frozen phonon from LDA calculations. The sample is 10% hole doping. The red line implies the Fermi level. [2]

In experimental researches, the PES has become one of the most important methods to study the electronic structure of molecules, solids and surfaces, since it can probe the occupied electron states directly. Fig. 3 is a skeptical illustration of the momentum specified PES and the multiple *e*-ph scattering process in a uniform system. As a soft x-ray shines, a photoelectron is emitted from the many-body system, leaving a hole in the solid. Generally, this hole state is not stable and immediately moves into other hole states with virtual excitations around it via interacting with nearby phonons (same as *e*-ph coupling). This is the so-called final state interaction [35]. If the coupling constant is zero, the spectral shape of the emitted photoelectron with a momentum p is the δ-function located at the energy ($\equiv \varepsilon_p$). After introducing the coupling, the created hole can emit a phonon with momentum $-q$, then be recoiled from ε_p to ε_{p+q} [Fig. 3 (c) and (d)], because of the momentum conservation rule. The electron energy thus changes to $\varepsilon_{p+q} + \omega_{-q}$ from the main peak ε_p [Fig. 3 (a) and (b)], a gain as a result of the energy conservation law. Certainly, this hole state can

continue to interact with other phonons, which thus arouses the multi-phonon scattering process.

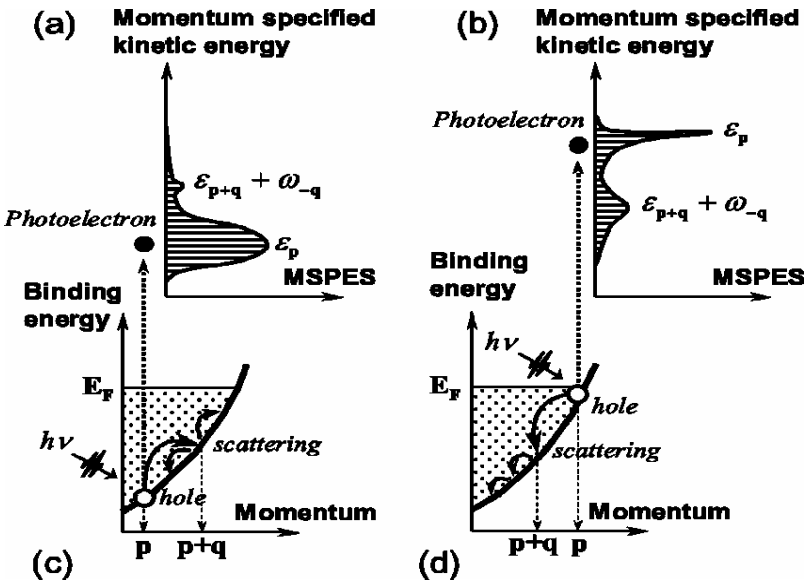

Fig. 3. MSPES and the multiple *e*-ph scattering process in a uniform system. In (c) and (d), a hole is created near the band bottom and the Fermi surface, respectively, by the photo-excitation, then scattered by phonons. The (a) and (b) are the corresponding spectral densities which can be detected directly in experiment. [17]

With the rapid development of the high resolution PES, some subtle structures and new phenomena have been detected. Related to the *e*-ph coupling problem, K. Ishizaka *et al.* [10] declared the observation of a satellite structure in the valence band PES (as quoted in Fig. 4) for the first time, when surveying heavily boron doped diamond sample. This structure is approximately in a periodic step-like shape with an energy interval about 0.16eV. Compared with the scanned Raman spectrum, it is assumed to be attributed to the strong *e*-ph coupling [10]. As mentioned before, the

phonon frequency of this mode also has been thought high of for the SC in Refs.2 and 7. At the same time, this periodic feature reminds us its similarity to the spectrum of localized electron model [18], wherein the interaction between electrons and the Einstein phonons characterizes the spectrum as separated δ-function like peaks with an equal energy interval. In this sense, it is natural to assume the step-like satellite structure originates from the *e*-ph coupling also.

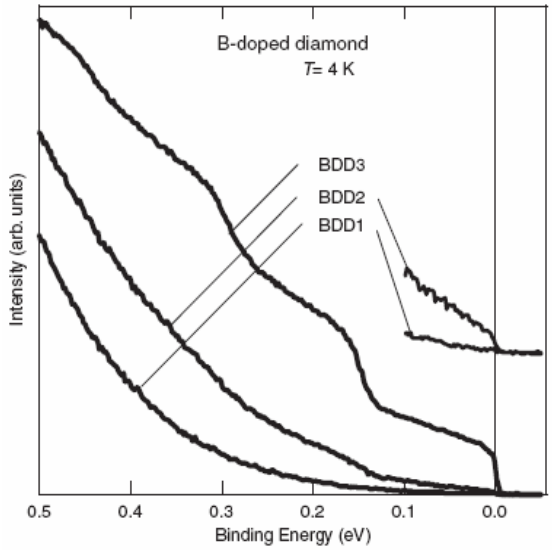

Fig. 4. PES of BDD thin films: BDD1 (n_B =3.5×10^{19}/cm³), BDD2 (1.75×10^{20}/cm^3), BDD3 (6.53×10^{21}/ cm^3).

It should also be noted that this multi-phonon structure has appeared, not in the well-known gap function of superconductivity, but in the photoemission spectrum of the normal state itself.

Except for the above character, there emerges a clear Fermi edge in heavily doped sample, which can not be found in lightly doped ones. This implies the material is undergoing semiconductor-metal transition on increasing the boron concentration to

certain level. The electrons can now tunnel from one boron atom to another, through the many carbon atoms in between, freely. In our opinion, the co-existence of a clear Fermi edge and the step-like satellite structure, observed in the PES experiment, is the very reflection of the co-existence of electron's two intrinsic attributes: itineracy and localization. Although ubiquitous, it seems quite unusual that this co-existence is detected so obviously and directly.

Then the problems what on earth the mechanism of this co-existence is, and what the function of *e*-ph coupling is in this co-existence, bring forward a challenge to the theory. Unfortunately, the coherent potential approximation (CPA) [21], a standard theory dealing with the disordered systems has some limitation in explaining the emergence of the Fermi edge, because it tacitly assumes the system remains uniform (every sites are regarded to be same: each virtually composed by two kinds of atoms in a given ratio.) after doping, which ensures the appearance of a Fermi edge at the very beginning, even in low doping case. While the local density functional (LDF) [2, 4-5] can not prove this step-like satellite structure successfully.

Here, we use a new path-integral theory developed by Nasu [22] to study the PES of the doped simple cubic lattice. This is based on many impurities Holstein model, which includes two characters. One is the coupling between electrons and Einstein phonons, usually called Holstein model [23]. The other is the disorder of the system. According to the Refs.8 and 14, the substitutional doping is the reasonable doping mode instead of the interstitial one. So, in our model, carbon atoms are randomly replaced by boron atoms according to the doping rate, with one less electron each doped site except for the potential change. It should be noted that, in the present

problem, the so-called randomness and the doped electron number are changed simultaneously, being different from both a simple randomness problem and a simple doping problem.

The main purpose of this study is to prove the co-existence of a Fermi edge and the phonon satellite structure by the electron's two intrinsic attributes theoretically, and clarify its mechanism, then to explain the experimental findings. We perform the path-integral by the Quantum Monte Carlo (QMC) simulation [24-26] in numerical calculations. Thus, it is completely free from any further approximation.

The below is the outline of this thesis. In chapter 2, we present the many impurities Holstein model, and apply the path-integral theory to calculate the one-body Green's function, from which the spectral function can be derived to compare with experimental data. Then Chapter 3 gives the numerical results and some discussions. Chapter 4 briefly summarizes this study.

Chapter 2: Model and Methods

We mean to clarify the experimental findings, i.e., to discuss the spectral density of an electron removed from (added into) an N-body system. According to the standard many-body theory, the one-body Green's function is required to obtain this spectral function, while conventional treatments of this Green's function usually invoke some perturbation theories [18]. Recently, Nasu [22] has developed a path-integral theory to study the optical response from the interacting many-body system. In this chapter, we apply this theory to our many impurities Holstein model to formulate the one-body Green's function, then to derive the spectral function.

§ 2.1 Many Impurities Holstein Model

As mentioned in Chapter 1, studying the effect of e-ph coupling, we employ the Holstein model [23], which is most simple to describe the interaction between electrons and Einstein phonons (site-localized lattice vibration). Meanwhile, the system under investigation is disordered. Carbon atoms are randomly substituted by impurity boron atoms according to a certain ratio, one less electron each doped site along with the potential change due to the replacement. Here, we provide the many impurities Holstein model, which includes both effects above.

Its Hamiltonian ($\equiv H$) is given as ($\hbar = 1$, throughout the work),

$$
\begin{aligned}
H \equiv & -t \sum_{<l,l'>} \sum_{\sigma} (a_{l\sigma}^{+} a_{l'\sigma} + h.c.) - \mu \sum_{l,\sigma} n_{l\sigma} + \Delta_e \sum_{l_0} \sum_{\sigma} n_{l_0\sigma} \\
& + \frac{\omega_0}{2} \sum_{l} (-\frac{\partial^2}{\partial Q_l^2} + Q_l^2) - S \sum_{l,\sigma} Q_l (n_{l\sigma} - \overline{n}_l / 2), \\
& n_{l\sigma} \equiv a_{l\sigma}^{+} a_{l\sigma} \ , \ \sigma = \alpha \ \text{or} \ \beta. \qquad (2\text{-}1)
\end{aligned}
$$

In the above equation, t is the transfer energy. $a_{l\sigma}^{+}$ ($a_{l\sigma}$) is the creation (annihilation) operator of a conduction electron with spin σ at site l. While in this model the electrons can hop just between the nearest neighboring sites expressed by $< l, l' >$. μ is the chemical potential of electrons. Δ_e denotes the potential difference between after and before doping, which determines the position of the impurity levels, as examined by many experiments [8, 27] on this material. The label l_0 means the randomly doped sites. S is the e-ph coupling constant. Q_l stands for the dimensionless coordinate operator for the phonon at site l with a frequency ω_0. $\overline{n}_l$ is the average electron number at site l. Hereafter, in order to simplify the problem, we take into account the coupling only at the doped sites, because in the pure diamond there is no strong evidence to show such phonon satellite structure in PES. It means that the coupling becomes important just after doping. This is also suggested by [5, 6], the boron atoms introduce localized vibrational modes significantly coupling with electrons. Making use of this, we can rewrite Eq. (2-1) into a simpler one as Eq. (2-2) by combining the parameters Δ_e and $\overline{n}_l$ together.

$$H \equiv -t \sum_{<l,l'>} \sum_{\sigma} (a_{l\sigma}^{+} a_{l'\sigma} + h.c.) - \mu \sum_{l,\sigma} n_{l\sigma} + \sum_{l_0,\sigma} n_{l_0\sigma} \Delta_e^{'}$$
$$+ \frac{\omega_0}{2} \sum_{l_0} (-\frac{\partial^2}{\partial Q_{l_0}^2} + Q_{l_0}^2) - S \sum_{l_0,\sigma} Q_{l_0} n_{l_0\sigma},$$
$$\Delta_e^{'} \equiv \Delta_e + S^2 \overline{n}_{l_0} / \omega_0. \qquad (2\text{-}2)$$

§ 2.2 Path-integral Theory

Using Trotter's decoupling formula

$$e^{-\theta H} = \lim_{L\to\infty} (e^{-\Delta H} \cdots e^{-\Delta H}),\ \theta = 1/(k_B T) \text{ and } \Delta = \theta / L, \qquad (2\text{-}3)$$

and inserting the phonon eigen-state $\left| x_{l_0} \right\rangle$, which is related to the operator Q_{l_0} and the eigen-value x_{l_0} by the eigen-equation

$$Q_{l_0} \left| x_{l_0} \right\rangle = x_{l_0} \left| x_{l_0} \right\rangle, \qquad (2\text{-}4)$$

we can get a path-integral form for the Boltzmann operator as below:

$$e^{-\theta H} \to \int \mathcal{D} x \left[T_+ \exp(-\int_0^{\theta} d\tau [h(\tau, x) + \Omega(\tau, x)]) \right.$$
$$\left. \times \prod_{l_0} [\, \left| x_{l_0}(\theta) \right\rangle \left\langle x_{l_0}(0) \right| \,] \right]. \qquad (2\text{-}5)$$

Here $h(\tau, x)$ and $\Omega(\tau, x)$ are listed below as

$$h(\tau,x) \equiv -t \sum_{<l,l'>} \sum_{\sigma} [a^{+}_{l\sigma}(\tau) a_{l'\sigma}(\tau) + a^{+}_{l'\sigma}(\tau) a_{l\sigma}(\tau)]$$

$$- \mu \sum_{l,\ \sigma} n_{l\sigma}(\tau) + \sum_{l_0,\sigma} n_{l_0\sigma}(\tau) \Delta_e^{'} - S \sum_{l_0,\sigma} x_{l_0}(\tau) n_{l_0\sigma}(\tau), \qquad (2\text{-}6)$$

$$\Omega(\tau,x) \equiv \sum_{l_0} \left\{ S x_{l_0}(\tau) \overline{n}_{l_0} + \frac{1}{2\omega_0} [\frac{\partial x_{l_0}(\tau)}{\partial \tau}]^2 + \frac{1}{2} \omega_0 x^2_{l_0}(\tau) \right\}. \qquad (2\text{-}7)$$

We should point out that the electric operators $a_{l\sigma}(\tau)$ and $n_{l\sigma}(\tau)$ in Eq. (2-6) have no real time-dependence. The time argument τ of these operators denotes only the time ordering T_+. While $x_{l_0}(\tau)$ is really time-dependent and is a c-number. $\mathcal{D}x$ means the summation over all possible $x_{l_0}(\tau)$, which depends on imaginary time τ and site l_0, and changes from $-\infty$ to $+\infty$. This is the so-called path-integral theory. Applying this, we can calculate the one-body Green's function.

Firstly, we define a $2N \times 2N$ path-dependent matrix $\mathbf{H}(\tau, x)$, whose elements are defined by

$$[\mathbf{H}(\tau,x)]_{j,j'} \equiv \langle 0 | a_j(\tau) h(\tau,x) a^{+}_{j'}(\tau) | 0 \rangle, \qquad (2\text{-}8)$$

where $|0\rangle$ is the true electron vacuum, and j symbolically substitutes site l and spin σ. It varies from 1 to $2N$. Then we define the time evolution operator $R(\tau, x)$ along a given path x as:

$$R(\tau, x) = T_+ \exp\left\{-\int_0^\tau d\tau' \mathbf{A}^+(\tau')\mathbf{H}[\tau', x(\tau')]\mathbf{A}(\tau')\right\},$$

$$\theta \geq \tau \geq 0, \tag{2-9}$$

where A^+ is a $2N$-dimensional vector operator given as

$$\mathbf{A}^+ \equiv (a_1^+, \cdots, a_j^+, \cdots, a_{2N}^+). \tag{2-10}$$

Corresponding to this operator $R(\tau, x)$, we also have the time evolution matrix:

$$\mathbf{R}(\tau, x) = T_+ \exp\left\{-\int_0^\tau d\tau' \mathbf{H}[\tau', x(\tau')]\right\}. \tag{2-11}$$

In terms of Boltzmann operator (2-5) and the time evolution operator Eq. (2-9), we define the free energy ($\equiv \Phi(x)$) along a given path $\boldsymbol{x}$ as

$$e^{-\theta\Phi(x)} = e^{-\int_0^\theta d\tau\, \Omega[\tau, x(\tau)]} \mathrm{Tr}[R(\theta, x)], \tag{2-12}$$

where the partition function ($\equiv$ Z) and the total free energy ($\equiv \Phi$) are given by

$$Z = e^{-\theta\Phi} = \int \mathcal{D}x\, e^{-\theta\Phi(x)}. \tag{2-13}$$

Accordingly, the expectation value of an operator ··· is obtained,

$$\langle \cdots \rangle = \frac{1}{Z} \int \mathcal{D}\, x e^{-\int_0^\theta d\tau\, \Omega[\tau, x(\tau)]} \mathrm{Tr}[R(\theta, x) \cdots]$$

$$= \frac{1}{Z} \int \mathcal{D}\, x\, e^{-\theta\, \Phi(x)} \langle \cdots \rangle_x , \qquad (2\text{-}14)$$

where $\langle \cdots \rangle_x$ means the expectation value along the path $\boldsymbol{x}$,

$$\langle \cdots \rangle_x = \mathrm{Tr}[R(\theta, x) \cdots] / \mathrm{Tr}[R(\theta, x)]. \qquad (2\text{-}15)$$

From the above definitions and notations, we can now write the one-body Green's function ($G(j\tau, j'\tau', \mathrm{x})$) of electrons in the given path $\boldsymbol{x}$ as

$$G(j\tau, j'\tau', x) = -sign(\tau - \tau') \left\langle T_+ \vec{a}_j(\tau) \vec{a}_{j'}^{+}(\tau') \right\rangle_x , \qquad (2\text{-}16)$$

where $\vec{a}_j(\tau)$ is the Heisenberg representation of a_j. It is really time-dependent, and defined as

$$\vec{a}_j(\tau) \equiv R^{-1}(\tau, x) a_j R(\tau, x). \qquad (2\text{-}17)$$

Then we can derive the differential equation of this operator $\vec{a}_j(\tau)$ as:

$$\frac{\partial \vec{a}_j(\tau)}{\partial \tau} = -\sum_k [\mathbf{H}(\tau, x)]_{jk} \vec{a}_k(\tau). \qquad (2\text{-}18)$$

The solution to this equation is given by

$$\vec{a}_j(\tau) = \sum_k [\mathbf{R}(\tau, x)]_{jk} a_k. \qquad (2\text{-}19)$$

Following the same procedure, we can also get

$$\vec{a}_j^{+}(\tau) = \sum_k a_k^{+} [\mathbf{R}^{-1}(\tau, x)]_{kj}. \qquad (2\text{-}20)$$

Now, the one-body Green's function along the path ***x*** can be written like this:

$$G(j\tau, j'\tau', x) = \sum_{k,k'} [\mathbf{R}(\tau, x)]_{jk} [\mathbf{R}^{-1}(\tau, x)]_{k'j'} \times \begin{cases} -\left\langle a_k a_{k'}^{+} \right\rangle_x, & \tau > \tau', \\ \left\langle a_{k'}^{+} a_k \right\rangle_x, & \tau < \tau', \end{cases} \qquad (2\text{-}21)$$

when $\tau > \tau'$, using the anti-commutation relation, $\left\langle a_k a_{k'}^{+} \right\rangle_x$ can be written as following:

$$\left\langle a_k a_{k'}^{+} \right\rangle_x = \delta_{kk'} - \left\langle a_{k'}^{+} a_k \right\rangle_x . \qquad (2\text{-}22)$$

Then, by using equations (2-15), (2-17) and (2-19), the term $\left\langle a_{k'}^{+} a_k \right\rangle_x$ is rewritten as:

$$\begin{aligned}\left\langle a_{k'}^{+} a_k \right\rangle_x &= \frac{\mathrm{Tr}[R(\theta,x) a_{k'}^{+} a_k]}{\mathrm{Tr}[R(\theta,x)]} = \frac{\mathrm{Tr}[a_k R(\theta,x) a_{k'}^{+}]}{\mathrm{Tr}[R(\theta,x)]} \\ &= \frac{\mathrm{Tr}[R(\theta,x) R^{-1}(\theta,x) a_k R(\theta,x) a_{k'}^{+}]}{\mathrm{Tr}[R(\theta,x)]} \\ &= \left\langle \vec{a}_k(\theta) a_{k'}^{+} \right\rangle_x = \sum_{k''} [\mathbf{R}(\theta,x)]_{kk''} \left\langle a_{k''} a_{k'}^{+} \right\rangle_x . \qquad (2\text{-}23)\end{aligned}$$

Combining the above equations (2-22) and (2-23), we get a matrix equation for $\left\langle a_{k''} a_{k'}^{+} \right\rangle_x$ as,

$$\delta_{kk'} = \sum_{k''} [1 + \mathbf{R}(\theta,x)]_{kk''} \left\langle a_{k''} a_{k'}^{+} \right\rangle_x , \qquad (2\text{-}24)$$

and its solution is obtained by:

$$\left\langle a_k a_{k'}^{+} \right\rangle_x = [\frac{1}{1 + \mathbf{R}(\theta,x)}]_{kk'} . \qquad (2\text{-}25)$$

When $\tau < \tau'$, we can get the solution for $\left\langle a_{k'}^{+} a_k \right\rangle_x$ in the same way.

Now, we have the expression for the Green's function along the given path ***x***,

$$G(j\tau, j'\tau', x) = \left[R(\tau, x) \begin{pmatrix} -\dfrac{1}{1+R(\theta, x)}, \tau > \tau' \\ \dfrac{1}{1+R^{-1}(\theta, x)}, \tau < \tau' \end{pmatrix} R^{-1}(\tau', x) \right]_{jj'} . \quad (2\text{-}26)$$

Considering all possible paths, the site-represented Green's function ($\equiv G_\sigma(ll', \tau)$) is finally obtained as

$$G_\sigma(ll', \tau) = \frac{1}{Z} \int \mathcal{D}x\, e^{-\theta\Phi(x)} G(l\sigma\tau, l'\sigma 0, x). \qquad (2\text{-}27)$$

Similarly, we can calculate the total number of electrons N_e of a system using

$$N_e = \frac{1}{Z} \int \mathcal{D}x\, e^{-\theta\Phi(x)} \mathrm{Tr}\left[\frac{1}{1+\mathbf{R}^{-1}(\theta, x)}\right]. \qquad (2\text{-}28)$$

When the electron number is fixed, the chemical potential μ can be determined by this relation.

To get the spectral density, it is usual to calculate the Fourier component corresponding to this site-represented dependant Green's function. However, since our system is not a uniform one, we can not do this type ARPES calculation. Still, we can make the use of the invariance of representation transformation to obtain the

ordinary one-body Green's function ($\equiv G_\sigma(\tau)$), by summing up this site-represented Green's function

($\equiv G_\sigma(ll',\tau)$) over sites,

$$G_\sigma(\tau) = \frac{1}{N}\mathrm{Tr}(G_\sigma(ll',\tau)) = \frac{1}{N}\sum_l \langle l | G_\sigma(ll,\tau) | l \rangle, \qquad (2\text{-}29)$$

and the spectral function $A_\sigma(\omega)$ then can be deduced from equation (2-29) through the analytic continuation

$$G_\sigma(\tau) = -\int_{-\infty}^{+\infty} \frac{e^{-\tau\omega}}{1+e^{-\tau\omega}} A_\sigma(\omega) d\omega. \qquad (2\text{-}30)$$

To compare with the PES experimental data, this spectral function is traditionally modified by the Fermi distribution ($f(\omega) = 1 / (e^{\theta\omega}+1)$) as

$$I(\omega) = \sum_\sigma A_\sigma(\omega) f(\omega), \qquad (2\text{-}31)$$

because only the occupied electronic states are probed.

§ 2.3 Numerical Methods

We perform two types of numerical calculations. The first one is the classical Monte Carlo (CMC) method, wherein the kinetic energy of phonons is neglected, and the Green's function is obtained by directly diagonalizing the electron Hamiltonian. In the second one, the site diagonal Green's function (Eq. (2-27)) is performed by the Quantum Monte Carlo (QMC) simulation. To increase the computing speed, we adopt the path updating method introduced by S. R. White *et al.* in Ref. 25. Though used to update electron spin configurations in the *e-e* coupling case, this method is applicable to our simulation after a slight revision. The computations become much rapid and stable than the standard Metropolis algorithm. Also, in order to avoid the numerical errors, we have applied the matrix factorization algorithm [28], wherein the so-called QDR decomposition is operated with the quad precision. We will explicate this method in detail in the Appendix A for the convenience of reading.

Before starting the measure, it is necessary to take enough sweeps to achieve a thermal equilibrium of the system. To reduce the correlation in the nearby measurements, we set an interval of adequate sweeps. Fig. 5 shows the basic principle of our QMC simulation. From the system equilibrium, it goes through all possible paths to get the expectation value of an operator. As shown in Fig. 5 (a), A_i is the value of an operator **A** in *i*-th path, and P_i is the occurrence probability of this path. Fig. 5 (b) is the path updating process in real calculations. Each impurity site of each time slice is updated (move or not) one after another according to the path updating method mentioned above.

In performing the analytic continuation to obtain the spectral function from the Green's function, we use the so-called "iterative fitting" method [17], which is proved to get converged result more rapid and stable than various other methods. Since this is mere mathematics and is not our original invention, its algorithm is only elaborated in the Appendix B.

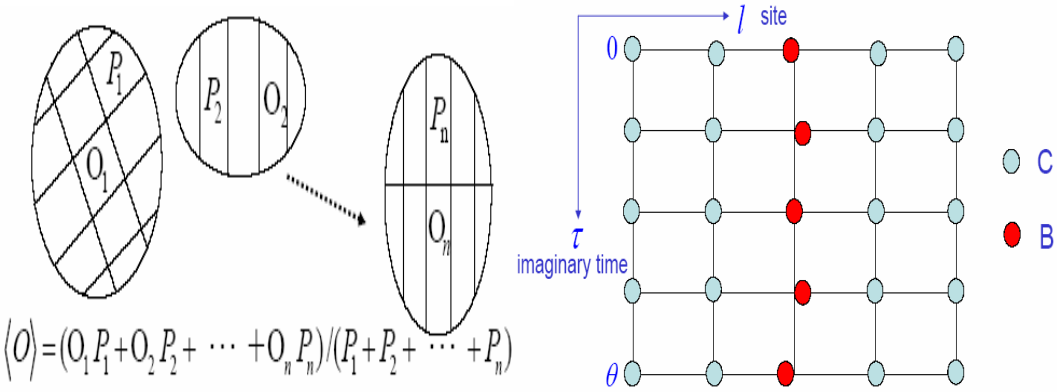

(a) (b)

Fig. 5. Schematic map shows the basic principle of QMC we use in calculation. (a) expectation value over all possible paths, as classic case does (b) updating phonon configuration in one possible path.

Chapter 3: Results and discussions

In this chapter, we will present our numerical results of the PES intensity function for a simple cubic lattice. Although the real diamond structure is much more complicated, it will not result in any essential difference.

The valence band of the pure diamond is fully filled. Being doped with boron, the material acts as *p*-type character with an impurity band about 0.37eV entering the band gap due to the potential difference between the two kinds atoms. Notice that we are interested in the energy region near the Fermi level (see Fig. 4), where the impurity band and the top of valence band lie around. Without paying much attention to the detail of the valence band natures faraway from the Fermi level, we can use this simple cubic structure to simulate the valence band of the real diamond crystal, focusing just on the area near the Fermi level in the PES spectra. Although using this simple structure, we are still able to reproduce the co-existence of a Fermi edge and the phonon satellite structure, which reflects the two intrinsic attributes of electrons.

Because we consider the *e*-ph coupling only at the doped sites, the phonon effect is not obvious in the whole system spectrum after averaging over all sites. So, we also present the doped sites spectrum.

Firstly, as a reference, we calculate the spectra for the simple cubic lattice with a single impurity, without regard to the *e*-ph coupling. The results are shown in Fig. 6, where the spectrum of the doped sites (red line) and the spectrum of whole system (green line) are given. From the doped sites spectrum, we can see the impurity level

lies a little above the top of valence band according to the experimental value 0.37eV. A long tail [29] due to the modulation of the impurity level by the valence band continuum extends almost the whole band, according to the so-called Fano effect [30].

Also, Ref. 28 gives a similar result when investigating a static single-site magnetic impurity system to explain the multiple peaks structure, as shown in Fig. 7 below. On each side, there is an impurity level, along with a Fano effect tail. The two tails overlap in the middle to form the third broad peak. Fig. 8 is a sketch of the Fano effect, which describes an isolated state, being modified by an admixture of continuum states, shifts a little and becomes asymmetric.

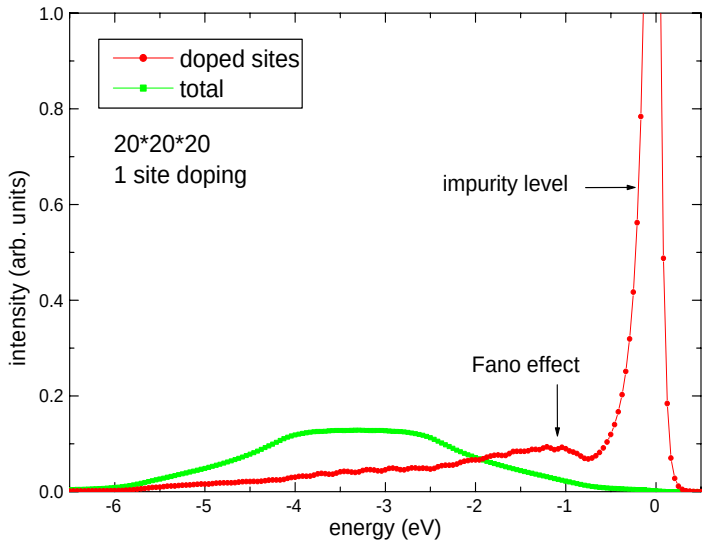

Fig.6. Photoemission spectra for a simple cubic crystal of a single impurity without *e*-ph coupling

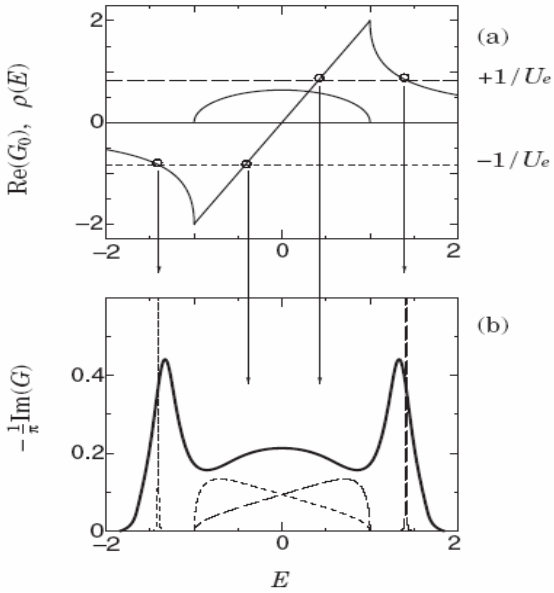

Fig. 7. Schematic illustration of the three peaks structure (thick line). (a) the lattice Green's function G_0 (solid lines), (b) the dashed and short dashed lines represent $-\mathrm{Im}(G)/\pi$.

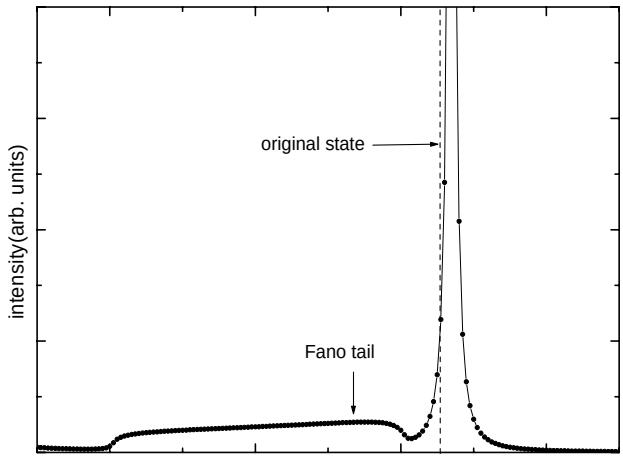

Fig. 8. Sketch map of the Fano effect: a single level is modulated by a continuum to shift a little and become asymmetric

Secondly, we increase the dopant concentration, and take the *e*-ph coupling into account. The spectra of different doping rates calculated by the CMC method are given in Fig. 9. Likewise, we distinguish the doped sites spectrum from the whole one at each rate. On increasing the doping ratio, we can clearly see in the whole spectra (green lines) the impurity band expands to fill the semiconductor gap, and then extends upto the top of the valence band. Thus, the semiconductor-metal transition occurs, and a clear Fermi edge emerges, as observed in Ref. 8. It is also confirmed by the local density functional (LDF) calculation [6]. While, the phonon satellite structure is absent in the present calculations since the phonons are classical. As discussed in the single impurity case, the impurity level is discrete a little above the top of the valence band. The electron can not move between the valence band and the impurity level because of the activation energy gap. On increasing the doping percentage, the impurity band overlaps with the top of the valence band to fill the gap gradually. Thus the electron can move freely from one impurity atom to another, by tunneling through those intermediate carbon atoms. Consequently, the material becomes a metal.

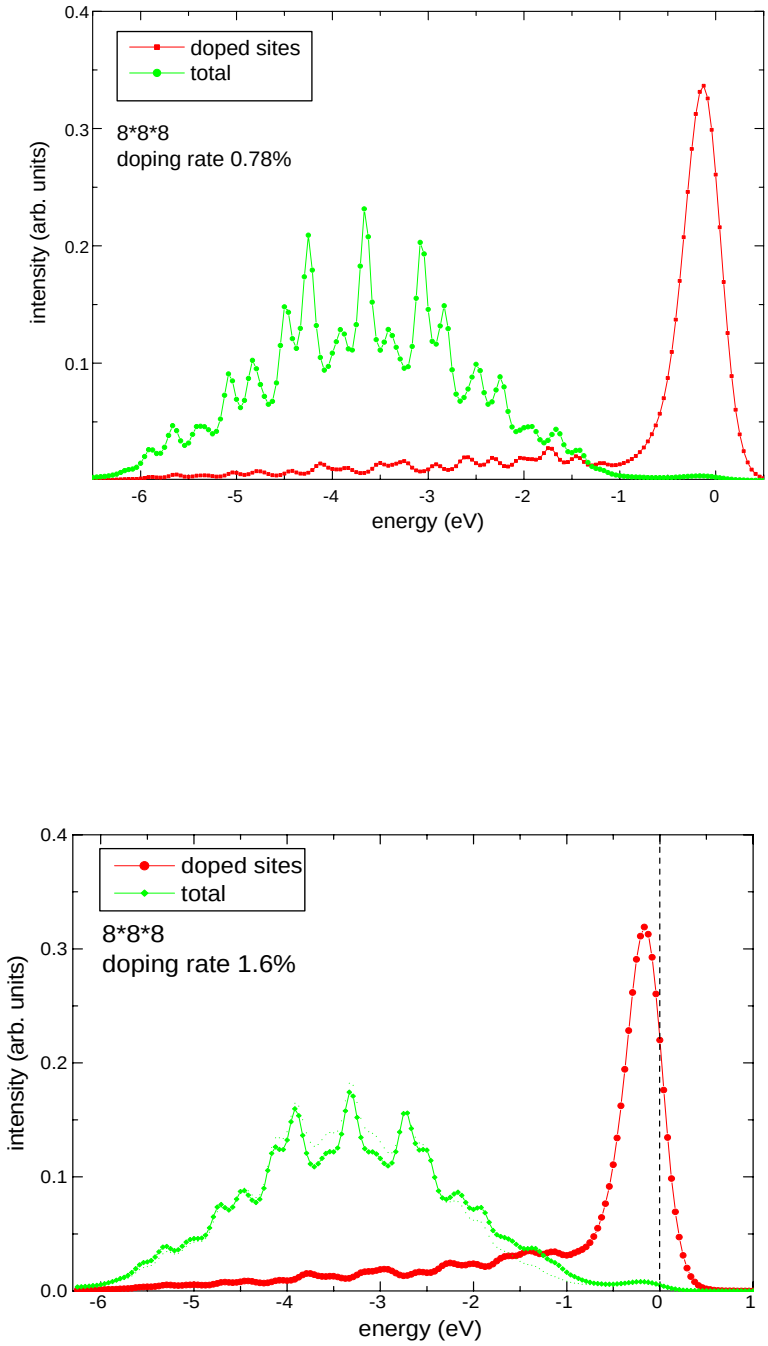

Fig. 9. Spectra of different doping rates using classic Monte Carlo method. The green lines are the whole system spectra, and the red ones are the doped sites spectra.

Finally, we perform the calculations by the QMC method, which is free from the approximation used in the CMC. The results are shown in Fig. 10.

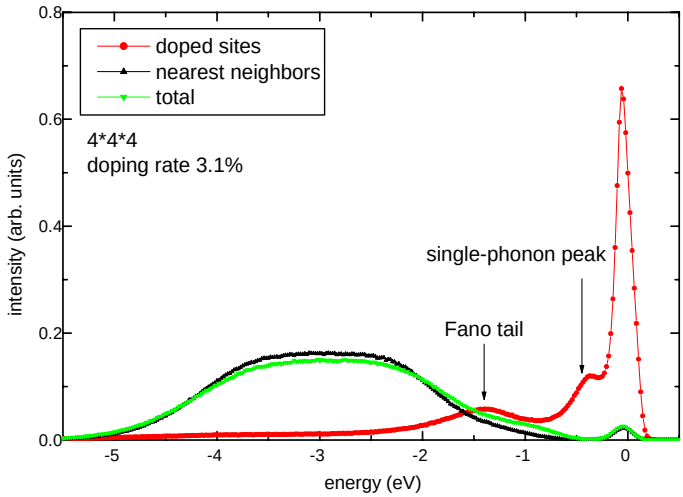

(a)

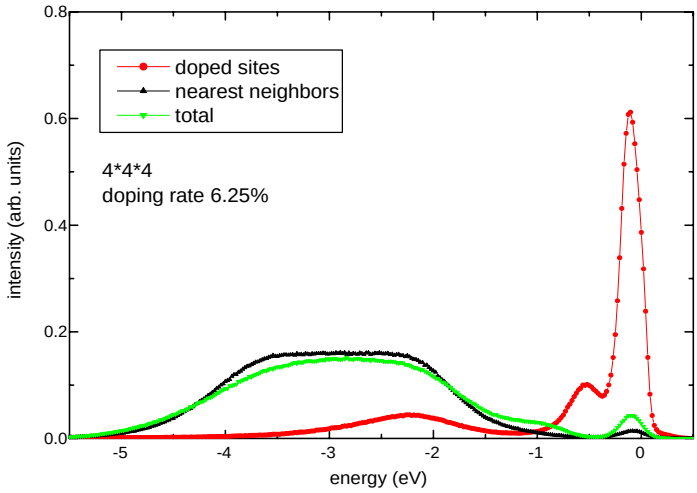

(b)

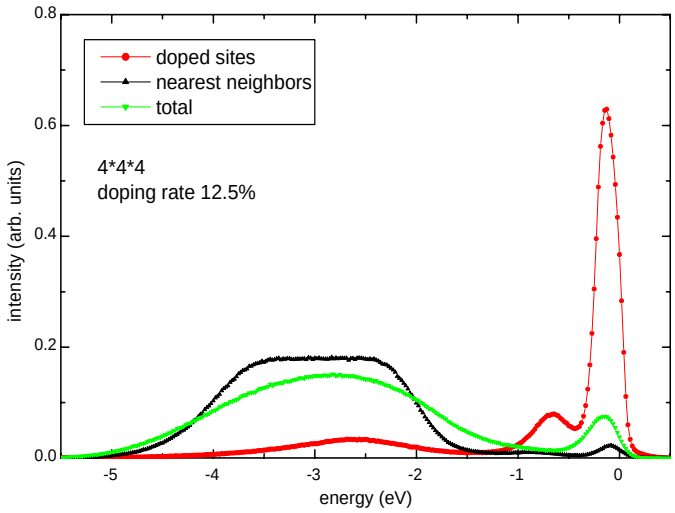

(c)

Fig. 10 the spectra of a simple cubic lattice with different doping rates using QMC method. The green lines are the whole system spectra. The red and the black denote the dopes sites and its nearest neighbor spectra, respectively.

In the doped sites spectra (red lines), except for the Fano effect tail, there is a notable shoulder-like structure a little below the main impurity peak. This is not found in the CMC cases, obviously coming from the phonon quantum character, even in relatively low doping samples. The doping ratios seem to be a little big, while the absolute number of doped sites is small because the system size is small, 4×4×4. As described in the Hamiltonian, the shoulder-like structure in the doped sites spectrum clearly reflects the process of the *e*-ph scattering. Here, we just use the bigger phonon energy (0.25eV), only for the sake of resolution in the numerical calculations. At the same time, the emergence of a Fermi edge is also observed clearly on the increase of

the doping rate.

As shown in Fig. 10, the phonon side peak lies at the very scope of the semiconductor gap, which means that this phonon peak from *e*-ph coupling can also contribute to the expansion of impurity band and the filling of the gap. In order to clarify the effect of *e*-ph coupling, we perform the computation of strong coupling S= 0.5eV changing from 0.25eV and the Einstein phonon frequency increases to 0.3eV. The results are shown below in Fig. 11. Another peak presents in the doped sites spectrum (red line) besides the Fano tail and the single-phonon peak. This peak is from the double-phonon, even multi-phonon scattering process as discussed in the introduction and Ref. 17. Also, the Fermi edge comes out, and in the whole system spectrum (green line), the step-like structure can be seen though obscure, which is zoomed around Fermi level in (b) to observe easily.

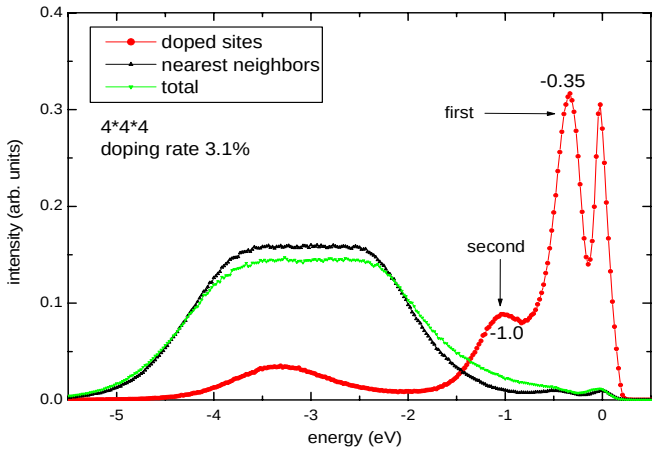

(a)

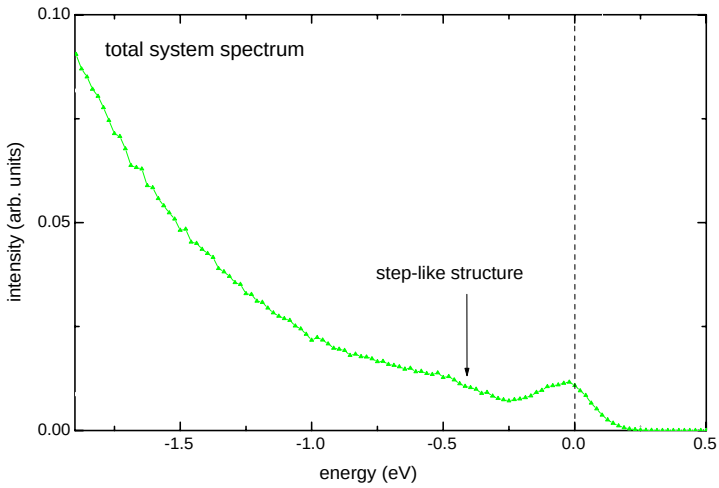

(b)

Fig. 11. the spectra of a simple cubic lattice on increasing the *e*-ph coupling constant using QMC method. (b) is just the zoomed area near Fermi level of (a) for the total system spectrum.

There seems to be a discrepancy between the positions of the phonon side peaks in Fig. 10 (red lines: (a) 0.3eV, (b) 0.5eV, (c) 0.6eV) and the ones expected from the phonon frequency we have used (ω_0=0.25eV). In a uniform system, the spectrum structure is determined by the simultaneous energy and momentum conservation of *e*-ph system. The energy interval ($\equiv\Delta\varepsilon$) between the neighboring phonon peaks is dependant not only on the phonon frequency, but also on the band shape as discussed in the introduction and Ref. 17. So that the phonon peaks usually do not distribute with an equal interval even when the phonon dispersion relation is constant. While in the localized electron model described by Mahan [18], the electron is pinned at one site and coupling with the Einstein phonons. So the self-scattering process

guarantees its spectrum as separated peaks with an equal energy interval of the phonon frequency. Our case is just between these two ends, comprising the characters from them. The phonon structure can not distribute with an equal interval exactly same as the phonon frequency, as detected by experiment [10]. Its periodicity is only approximately. At the same time, the shape of this phonon side peak is not discrete δ-function like peaks unlike the localized electron model [18], because it is also modulated to be asymmetric and a little shifts from the original position, according to the so-called Fano effect as shown in Fig. 8.

By now, we have proved the co-existence of a Fermi edge and the phonon satellite step-like structure using a simple cubic lattice. Due to the *e*-ph coupling and the increase of the doping rate, the impurity band expands upto the top of the valence band, thus fills the activation energy gap gradually. The electrons can itinerate from one impurity atom to another one, by tunneling through those intermediate carbon atoms freely, and the material becomes a metal. At the same time, the electrons are localized by coupling with the Einstein phonons, which makes the spectrum show approximately periodic step-like shape.

Here, we should mention that we have one more advantage over CPA. As we have done, we can distinguish the spectra of different kinds of atoms in the material, being very useful to explain resonance PES experiments directly, though there is no such kind of experiments performed yet. The resonance photoemission means tuning the incident photon energy to stimulate a core-level absorption excitation. Then the possible immediate Auger decay can lead to a final state with emitting an Auger electron. This final state is identical to a certain direct photoemission final state. The

coherence of the final states from direct PE and Auger effect leads to a characteristic variation of the photoemission intensity with the photon energy, according to so-called Fano line-shape [30]. This feature can be used for the assignment of band structures to different chemical components in the solid. Fig. 12 simply shows the comparison of this resonance PES process with the direct PES mentioned above. Because the excitation energy from core level 1s to top of valence band (TVB) is different between carbon (about 284eV) and boron (about 190eV), it is natural to get the PES of boron firstly, then carbon by tuning the incident photon energy to match these values.

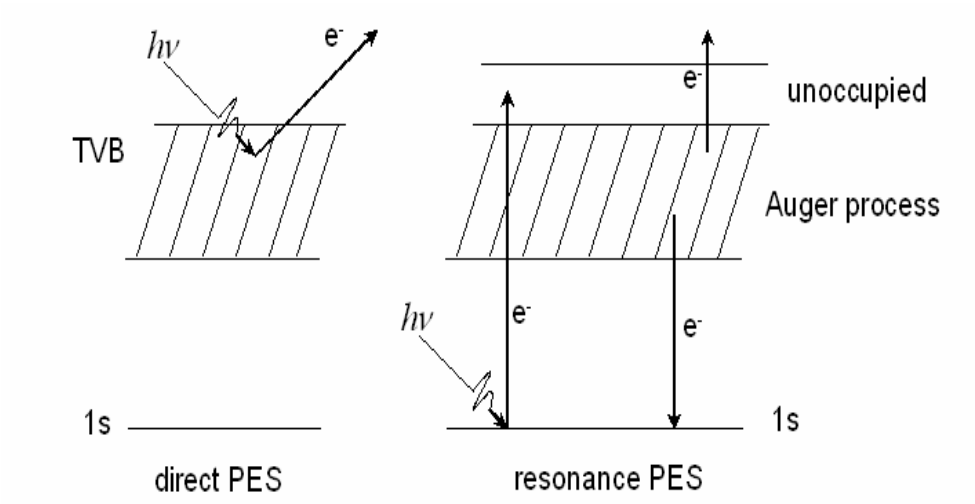

Fig. 12. An illustration of comparing resonance PES with direct PES

Chapter 4: Conclusions

In this work, we have applied the newly developed path-integral theory to the many impurities Holstein model to investigate the two intrinsic attributes of electrons: itineracy and localization. This can clarify the co-existence of a Fermi edge and the step-like satellite structure detected in PES of boron-doped diamond recently. Focusing on the area close the Fermi level, we just use a simple cubic lattice structure to simulate the various valence band natures of BDD to simplify the problem without losing the key points.

From the classical computation, we can clearly see the emergence of a clear Fermi edge on increasing the doping ratio. The impurity band expands upto the top of valence band, and fills the semiconductor gap gradually. Thus, the sample undergoes a semiconductor-metal transition, and electrons can move freely from one impurity atom to another one through the intermediate carbon atoms. In quantum Monte Carlo simulations, the lattice Green's function is calculated by the path-integral theory to reproduce the spectral function. From the whole system spectrum, the phase transition is reconfirmed on the increase of the dopant concentration. The satellite structure is observed in the doped sites spectrum, even within lightly doped samples. This structure has not been found in CMC case, obviously coming from the phonon quantum character in the *e*-ph coupling. Increasing the coupling constant, a second phonon peak also presents corresponding to the double-phonon, even multi-phonon scattering process. Because of the strong coupling, a clear Fermi edge appears though

the doping rate is low. In summary, due to the *e*-ph coupling and the increase of the dopant concentration, the impurity band expands to fill the semiconductor gap, and then overlaps with the top of the valence band gradually. A clear Fermi edge comes out and the phase transition occurs, which reflects the free itineracy of electrons. At the same time, the *e*-ph coupling results in the localization of electrons, exhibiting as a shoulder-like satellite structure in the doped sites spectrum. This co-existence of the two basic properties of electron: itineracy and localization qualitatively interprets the co-existence of a Fermi edge and the step-like satellite structure detected by the PES experiment of BDD [10].

At the same time, our method, which can distinguish the spectral functions of different components in material as we have done in calculating the spectra for the impurity atoms, the nearest neighboring atoms and the whole system respectively, is quite useful to clarify resonant PES experiments.

Acknowledgements

I would like to give my deepest appreciation to my supervisor, Professor Keiichiro Nasu. He has provided me with this valuable chance to study in Japan. Also, under his guidance and encouragement, I can develop me knowledge and experience, and finally accomplish this research. I also would like to send my appreciation to my graduate advisor Professor Changqin Wu for many inspiring discussions and recommending me for this advanced study. I would like to thank Dr. K. Ji for his helpful suggestions and discussions about the research. My acknowledgement is extended to Dr. K. Iwano, Dr. N. Keita and Mr. R. Lukas for constructing the computing facilities and many helps in daily life. At last, I express special thanks to my family, without their support and trust, it would be impossible for me to complete my study for these three years.

Appendix A: Matrix Factorization Technique

In this part, we show the matrix factorization technique in calculating the one-body Green's function accurately. Since in Ref. 28, the details of this matrix decomposition procedure have been explained, we just pick up its important points here. As having written in Eq. (2-11), we define the time evolution matrix $\mathbf{R}(\tau, x)$:

$$\begin{aligned}\mathbf{R}(\tau, x) &= T_{+}\exp\left\{-\int_0^{\tau} d\tau'\,\mathbf{H}[\tau', x(\tau')]\right\} \\ &= e^{-\Delta\tau\mathbf{H}(\tau_l, x)} e^{-\Delta\tau\mathbf{H}(\tau_{l-1}, x)} \cdots e^{-\Delta\tau\mathbf{H}(\tau_1, x)} \\ &= \mathbf{C}_l \mathbf{C}_{l-1} \cdots \mathbf{C}_1 \quad (1 \le l \le L), \end{aligned} \tag{A-1}$$

$$\mathbf{C}_l = e^{-\Delta\tau\mathbf{H}(\tau_l, x)}. \tag{A-2}$$

Then the time evolution matrix $\mathbf{R}(\tau, x)$ is given by the products of matrix serial $\mathbf{C}_l$.

As well known, in order to avoid the numerical error in these products of matrices, the matrix factorization technique based on the Gram-Schmidt orthogonalization procedure has been developed. Applying this technique, we perform this calculation as follows:

$$\mathbf{R}(\tau, x) = \mathbf{C}_l \cdots \mathbf{C}_{2m} \cdots \mathbf{C}_{m+1} \underbrace{\mathbf{C}_m \cdots \mathbf{C}_1}_{m}, \tag{A-3}$$

and the product of m matrices $\mathbf{C}_l$ from the right end is calculated firstly like this:

$$\mathbf{C}_m \cdots \mathbf{C}_1 = \mathbf{Q}_1 \mathbf{D}_1 \mathbf{R}_1 . \qquad \text{(A-4)}$$

Here, $\mathbf{Q}_i$, $\mathbf{D}_i$ and $\mathbf{R}_i$(i=1, 2, ···, l/m) represent the orthogonal, diagonal, and unit right triangular matrices, respectively. We repeat this procedure l/m times from the right end

$$\begin{aligned}
\mathbf{R}(\tau, x) &= \mathbf{C}_l \cdots \underbrace{(\mathbf{C}_{2m} \cdots \mathbf{C}_{m+1} \mathbf{U}_1)} \mathbf{D}_1 \mathbf{R}_1 \\
&= \mathbf{C}_l \cdots \mathbf{U}_2 \mathbf{D}_2 \mathbf{R}_2 \mathbf{R}_1 \\
&= \mathbf{C}_l \cdots \mathbf{U}_2 \mathbf{D}_2 \mathbf{R}'_2 \\
&\quad \vdots \\
&= \mathbf{U}_{l/m} \mathbf{D}_{l/m} \mathbf{R}_{l/m} . \qquad \text{(A-5)}
\end{aligned}$$

In this form, only the diagonal matrix $\mathbf{D}_i$ has large variations in the size of its elements. In the above calculation from the first line to the second one, we first multiply the matrices in the parentheses, the multiply it to $\mathbf{D}_1$. The latter multiplication only rescales the columns of the matrix, and does not produce the numerical instability. Therefore, we can confine the unstable portion only in $\mathbf{D}_i$.

Appendix B: Iterative Fitting Method

As discussed before, we are able to calculate the one-body Green's function at discrete imaginary time points within the quantum Monte Carlo method. While we want to investigate the band character, the photoemission spectrum should be derived from this imaginary time Green's function by the analytic continuation of Eq. (2-30). But in the numerical calculation, it usually starts from the following equation,

$$G_i = \sum_j K_{ij} A_j \Delta \omega, \tag{B-1}$$

where i and j denote imaginary time τ and frequency ω, respectively, and

$$K_{ij} = -\frac{e^{-\tau_i \omega_j}}{1 + e^{-\tau_i \omega_j}}, \tag{B-2}$$

is the integral kernel (We just leave off spin and momentum indices for convenience.). The summation in Eq. (B-1) covers the region where A_j is not zero, and the Green's function G_i is obtained from QMC simulation. Since the QMC data are subject to the noise with root-mean-square error σ, the spectrum is usually obtained by minimizing the misfit function χ^2 with respect to A_j

$$\chi^2 = \sum_i \frac{1}{\sigma_i^2}\left[G_i - \sum_j K_{ij} A_j \Delta\omega\right]. \qquad \text{(B-3)}$$

Though spectrum A_j can be easily obtained by solving Eq. (B-1) or minimizing Eq. (B-3), the positivity and smoothness of the spectral function are susceptible to be damaged due to numerical error and intrinsic nonlinearity of the kernel K_{ij}, resulting in unphysical structure with negative values or vibrating shape. To tackle this difficulty, auxiliary function or parameter should be attached with χ^2 when preceding with the numerical inversion. There are some methods [31, 32, 33] invented according to this idea, but the least square fitting method [31] has no self-consistent criterion for choosing parameters or with the maximum entropy method [32, 33], the inversed spectrum has been noticed to strongly dependent on the way of selecting parameters [34].

In our numerical calculation, we use the iterative fitting method [17] to perform the analytic continuation. It can self-consistently derive the positive-definite, smooth spectrum from the Green's function independent of any auxiliary function or parameter. Here, we just show the main idea of this method.

Its algorithm is based on the sum rule of the spectral function [18],

$$\sum_j A_j \Delta\omega = 1, \qquad \text{(B-4)}$$

which suggests that the spectral function can be rewritten into an iterative form

$$A_j^{(N)} = \frac{n_j^{(N)}}{N\Delta\omega}, \qquad \text{(B-5)}$$

where $n_j^{(N)}$ is the bin counter corresponding to $A_j^{(N)}$ and records the times of the ***j***-th bin being used during the previous N iterative steps. Now the sum rule (B-4) is fulfilled by

$$N = \sum_j n_j^{(N)}, \qquad \text{(B-6)}$$

and the positive limit of $A_j^{(N)}$ is also guaranteed because the counter $n_j^{(N)}$ is always nonnegative.

To obtain the spectral function, we originate from a flat spectrum, then repeat the following procedure:

(1) Calculate the Green's function $G_i^{(N)}$ using the present spectral function $A_j^{(N)}$

$$G_i^{(N)} = \sum_j K_{ij} A_j^{(N)} \Delta\omega, \qquad \text{(B-7)}$$

(2) Measure the distance ($\equiv\chi^{(N)}$) between $G_i^{(N)}$ and the true one G_i (QMC result) as

$$[\chi^{(N)}]^2 = \sum_i [G_i^{(N)} - G_i]^2, \qquad \text{(B-8)}$$

which finally should be minimized by the iteration.

(3) Make a trial spectral function $A_j^{(N+1)}$ of the next step N+1, whose $n_j^{(N+1)}$ is different from $n_j^{(N)}$ by only one, and only in a randomly selected bin j_0 ,

$$n_j^{(N+1)} = n_j^{(N)} + \delta_{jj_0}. \qquad \text{(B-9)}$$

By this trial, we have new $A_j^{(N+1)}$, $G_i^{(N+1)}$ and then $[\chi^{(N+1)}]^2$.

(4) Check the difference $\boldsymbol{S}$ defined as

$$S = [\chi^{(N)}]^2 - [\chi^{(N+1)}]^2 + \sum_i [G_i^{(N+1)} - G_i^{(N)}]^2. \qquad \text{(B-10)}$$

(5) If $\boldsymbol{S} > 0$ then accept the trial move Eq. (B-9), and repeat a new cycle from step (1). Otherwise, reject this trial move Eq. (B-9) and return to step (3). The meaning of $\boldsymbol{S}$ of Eq. (B-10) is explained in Fig. 13. In Eq. (B-8), $\chi^{(N)}$ gives the distance from the true $\mathbf{G}$ to the trial $\mathbf{G}^{(N)}$, in a hyperspace spanned by various $\mathbf{G}$'s, $\mathbf{G}^{(N)}$'s, and $\mathbf{G}^{(N+1)}$'s, as schematically shown in Fig. 13. The sphere is also symbolically denoted by $\boldsymbol{S}_1$ in the figure. If $\chi^{(N)} > \chi^{(N+1)}$, or as same $\mathbf{G}^{(N+1)}$ is in the sphere $\boldsymbol{S}_1$, which means the distance becomes shorter than before, we have to accept this kind of moves of Eq. (B-9) to close to the true Green's function.

While, sometimes $\chi^{(N)}$ may not be a so simple function of this move (≡**Δ**):

$$\mathbf{\Delta} = \mathbf{G}^{(N+1)} - \mathbf{G}^{(N)}, \qquad \text{(B-11)}$$

instead it will be a nonlinear and complicated function. In some cases, $\chi^{(N)}$ is in a local minimum with respect to the move **Δ**, and this move can never make the distance shorter. For these reasons, in Eq. (B-10), this method introduces a "relaxation effect" through the third term, which avoids the search for $\chi_{\min}^{(N)}$ being trapped in such a local minimum. Since the projection of **Δ** on the vector $\mathbf{G}^{(N)}$–**G** is just $-\boldsymbol{S}/2\chi^{(N)}$, the acceptable region for the trial $\mathbf{G}^{(N+1)}$ can be found to be (i) and (ii) in Fig. 13, both of which correspond to $\boldsymbol{S} > 0$. By the second region (ii), the minimization is relaxed, and thus an uphill search for a more global minimum becomes possible.

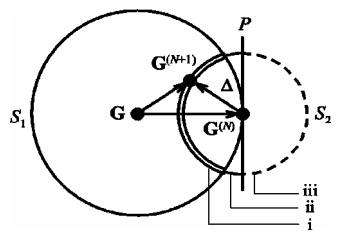

Fig. 13. Schematic interpretation for the recipe of analytic continuation. The hyper sphere $\boldsymbol{S}_1$ is centered at **G** with radius $\chi^{(N)}$, and $\boldsymbol{S}_2$ is centered at $\mathbf{G}^{(N)}$ with radius |**Δ**|. Three regions are labeled (i) acceptance region of shorter distance, (ii) acceptance region for minimum relaxation even of longer distance, and (iii) rejection region. [17]

Bibliography

[1] E.A. Ekimov *et al.*, Nature (London) 428 (2004) 542

[2] L. Boeri, J. Kortus and O.K. Andersen, Phys. Rev. Lett. 93 (2004) 237002

[3] K.W. Lee and W.E. Pickett, Phys. Rev. Lett. 93 (2004) 237003

[4] Y. Ma *et al.*, Phys. Rev. B 72 (2005) 014306

[5] X. Blase, Ch. Adessi and D. Connétable, Phys. Rev. Lett. 93 (2004) 237004

[6] H.J. Xiang *et al.*, Phys. Rev. B 70 (2004) 212504

[7] F. Giustino *et al.*, Phys. Rev. Lett. 98 (2007) 047005

[8] J. Nakamura *et al.*, Phys. Rev. B 70 (2004) 245111

[9] J. Nakamura, T. Oguchi *et al.*, cond-mat/0410144

[10] K. Ishizaka *et al*, Science and Technology of Advanced Materials 7 (2006) S17-S21

[11] T. Yokoya *et al*, Science and Technology of Advanced Materials 7 (2006) S12-S16

[12] K.W. Lee and W.E. Pickett, Phys. Rev. B. 73 (2006) 075105

[13] T. Shirakawa *et al.*, J. Phys. Soc. Jpn. 76 (2007) 014711

[14] T. Oguchi, Science and Technology of Advanced Materials 7 (2006) S67-S70

[15] G. Baskaran Science and Technology of Advanced Materials 7 (2006) S49-S53

[16] G.L. Zhao *et al.*, private discussions

[17] K. Ji, H. Zheng and K. Nasu, Phys. Rev. B 70 (2004) 085110

[18] G. D. Mahan, *Many-Particle Physics* 3rd ed. (Plenum, New York, 2000)

[19] A. Zunger, A.J. Freeman, Phys. Rev. B 15 (1977) 5049

[20] A.T. Collins, A.W.S. Williams, J. Phys. C 4 (1971) 1789

[21] P. Soven Phys. Rev. 156 (1966) 3

[22] K. Nasu, J. Phys. Soc. Jpn. 65 (1996) 2285

[23] T. Holstein, Ann. Phys. (N.Y.) 8 (1959) 325

[24] D. P. Landau, K. Binder, *A Guide to Monte Carlo Simulations in Statistical Physics* (Cambridge university press 2000)

[25] S. R. White *et al.*, Phys. Rev. B 40 (1989) 506

[26] R. Blankenbecler *et al.*, Phys. Rev. D 24 (1981) 2278

[27] J. W. Glesener, Appl. Phys. Lett. 64 (1994) 217

[28] M. Yamazaki *et al.*, J. Phys. Soc. Jpn. 72 (2003) 611

[29] K. Cho, Y. Toyozawa, J. Phys. Soc. Jpn. 30 (1971) 1555

[30] U. Fano, Phys. Rev. 124 (1961) 1866

[31] S.R. White *et al.*, Phys. Rev. Lett. 63 (1989) 1523

[32] J. Skilling and R.K. Bryan, Mon. Not. R. Astron. Soc. 211 (1984) 111

[33] J.E. Gubernatis and M. Jarrell, Phys. Rep. 269 (1996) 135

[34] J.E. Gubernatis *et al.*, Phys. Rev. B 44 (1991) 6011

[35] S. Hüfner, *Photoelectron Spectroscopy* third edition (Springer 2003)

Papers

Here, the first is the full text of a paper co-authored with Prof. Nasu during applying for this doctoral thesis study. The others are the papers published or to be published during this study period.

Breather in the motion of a polaron in an electric field

J. F. Yu,[1] C. Q. Wu,[1,*] X. Sun,[1] and K. Nasu[2]
[1]*Research Center for Theoretical Physics, Fudan University, Shanghai 200433, China*
[2]*Institute of Materials Structure Science, KEK, Tsukuba, Ibaraki 305-0801, Japan*
(Received 19 January 2004; revised manuscript received 12 May 2004; published 24 August 2004)

It has been known that a charged polaron will reach a constant speed after being accelerated only for a short time in an electric field. Within a dynamical nonadiabatic evolution method, we simulate the motion of polaron under the influence of the electric field which is present for different periods. We find the lattice oscillation behind the polaron will be localized and separated with the moving polaron once the electric field is turned off. It is shown that the localized lattice oscillation is nothing but a breather, specifically, a moving multibreather excitation. Furthermore, it is the breather which bears the incresed energy due to the electric field acting on the polaron, so that the polaron can move at a constant speed even in the presence of an electric field.

DOI: 10.1103/PhysRevB.70.064303 PACS number(s): 71.38.−k, 72.80.Le, 72.15.Nj, 71.23.An

I. INTRODUCTION

Recent years, organic electronic devices, e.g., light-emitting diodes, and, field-effect transistors, are attracting considerable interest because they have processing and performance advantages for low-cost and large-area applications.[1] In these devices, organic polymers are used as the light-emitting and charge-transporting layers, in which the electron and/or hole are injected from the metal electrodes and transported under the influence of an external electric field. Due to the strong electron-lattice interactions, it is well known that additional electrons or holes in conjugated polymers will induce self-localized excitations, such as solitons[2] (only in *trans*-polyacetylene) and polarons.[3] As a result, it has been generally accepted that the charge carriers in conjugated polymers are these excitations including both charge and lattice distortion.[4]

There have been extensive studies on soliton and polaron dynamics in conjugated polymers[5–8] under the influence of external electric fields. It is shown that solitons as well as polarons keep their shape while moving along a chain. Solitons are shown to have a maximum velocity $2.7v_s$, where v_s is the sound velocity.[6,9] The situation will be different for polarons, which has been shown to be not created in electric fields over 6×10^4 V/cm due to the charge moving faster and not allowing the distortion to occur.[7] A recent study by Johansson and Stafström[8] deals with the polaron migration between neighboring polymer chains. The numerical results show that the polaron becomes totally delocalized, either before or after the chain jump for the electric field over 3×10^5 V/cm. A preexisted polaron in a single chain can survive under the field up to 10^6 V/cm.[10,11]

While the stability of polaron motion under an external electric field has been discussed, we will concentrate on the phonon excitation due to the motion of polaron under the influence of a moderate electric field in this paper. The work is motivated by the observation that a charged polaron will reach a constant speed after being accelerated only for a short time under an electric field.[7,8] Within a dynamical nonadiabatic evolution method,[6] we simulate the motion of polaron under the electric field which is present for different periods. We find the lattice oscillation behind the polaron will be localized and separated with the moving polaron once the electric field is turned off. It is shown that the localized lattice oscillation is nothing but a discrete breather, which has been a subject in nonlinear systems for more than a decade (see, e.g., Refs. 12–14). Furthermore, it is pointed out that it is the breather which bears the increased energy due to the electric field acting on the polaron, so that the polaron can move at a constant speed even in the presence of the field.

The paper is organized as follows. In the following section, we present a tight-binding one-dimensional model for a polymer chain under the influence of an external electric field and describe the dynamical evolution method. Main results are presented in Sec. III and the discussion and summary of this paper are given in Sec. IV.

II. MODEL AND METHOD

The model Hamiltonian we consider for a polymer chain in this paper takes the following form:[2,6]

$$H = H_e + H_{\mathrm{latt}}. \tag{1}$$

The electronic part is

$$H_e = -\sum_{n,\sigma} t_n[e^{-i\gamma A(t)}c^{\dagger}_{n+1,\sigma}c_{n,\sigma} + \mathrm{H.c.}], \tag{2}$$

where $t_n[\equiv t_0-\alpha(u_{n+1}-u_n)]$ is the hopping integral between sites n and $n+1$ with α being electron-lattice coupling constant and u_n being the monomer displacement of site n from its undimerized equilibrium position, $c^{\dagger}_{n,\sigma}$ ($c_{n,\sigma}$) is the creation (annihilation) operator of an electron with spin σ at site n, the parameter γ is defined as $\gamma=ea/\hbar c$ with e being the absolute value of the electronic charge, a the lattice constant, and c the light velocity, and $A(t)$ is the time dependent vector potential being related with the electric field $E(t)$ along the chain direction as $E(t)=-(1/c)\partial A(t)/\partial t$. The lattice part is

$$H_{\mathrm{latt}} = \frac{K}{2}\sum_n (u_{n+1}-u_n)^2 + \frac{M}{2}\sum_n \dot{u}_n^2, \tag{3}$$

where K represents the force constant originated from the σ-bond between carbon atoms and M the mass of a site, such

as that of a CH-unit for *trans*-polyacetylene.

In this work, we consider a chain of N-monomer with periodic boundary condition, and N is taken to be large enough, such as 300 or 200 in some cases. Other model parameters are those generally accepted for *trans*-polyacetylene:[2] $t_0=2.5$ eV, $K=21.0$ eV/Å^2, $\alpha=4.1$ eV/Å, $a=1.22$ Å, and $M=1349.14$ eV fs^2/Å^2. Before we go further for the dynamical evolution, we determine the static structure of a polaron in the absence of an external electric field.

The total energy is obtained by the expectation value of the Hamiltonian (1) at the ground state $|g\rangle$,

$$E_t = \langle g|H_e|g\rangle + \frac{K}{2}\sum_n (u_{n+1}-u_n)^2. \tag{4}$$

The electronic states are determined by the electronic part of the Hamiltonian (2) and the lattice configuration of the polymer $\{u_n\}$ is determined by the minimization of the total energy in the above expression

$$u_{n+1}-u_n = -\frac{\alpha}{K}(\rho_{n,n+1}+\rho_{n+1,n})+\lambda, \tag{5}$$

where λ is a Lagrangian multiplier to guarantee the polymer chain length unchanged, i.e., $\Sigma_n(u_{n+1}-u_n)=0$. $\rho_{n,n'}$ is the element of density matrix, which will be given below. The initial configuration of a polaron in the following dynamical evolution will be chosen from the solution of the above self-consistent Eq. (5) at the ground state where the electronic band is half-filled with one more electron.

Now, we describe the nonadiabatic dynamical method that has been used for the dynamics of soliton[6] and polaron[7,8] in an electron-lattice interacting system. The evolution of the electron wave functions depends on the time-dependent Schrödinger equation

$$i\hbar\dot{\phi}_{n,\mu}(t) = -t_{n-1}e^{-i\gamma A}\phi_{n-1,\mu}(t) - t_n e^{i\gamma A}\phi_{n+1,\mu}(t). \tag{6}$$

The lattice displacements are determined classically by the following Newtonian equations of motion:

$$\begin{aligned} M\ddot{u}_n(t) = {} & K[u_{n+1}(t)+u_{n-1}(t)-2u_n(t)] \\ & + \alpha e^{-i\gamma A}[\rho_{n,n-1}(t)-\rho_{n+1,n}(t)] \\ & + \alpha e^{i\gamma A}[\rho_{n-1,n}(t)-\rho_{n,n+1}(t)], \end{aligned} \tag{7}$$

where $\rho_{n,n'}$ is the element of the density matrix defined as

$$\rho_{n,n'}(t) = \sum_\mu \phi^*_{n,\mu}(t) f_\mu \phi_{n',\mu}(t), \tag{8}$$

where f_μ is the time-independent distribution function determined by initial occupation (being 0, 1, or 2). The coupled differential Eqs. (6) and (7) can be solved numerically by use of the same technique in Refs. 6 and 8. The time step is chosen to be as small as 0.1 fs to avoid numerical errors.

In the real calculation, we choose the external field to be turned on smoothly, that is, we let $E(t)=E_0\exp[-(t-t_c)^2/t_w^2]$ for $0<t<t_c$, $E(t)=E_0$ for $t_c<t<t_{\rm off}$, and $E(t)=0$ for $t>t_{\rm off}$ with t_c being a smooth turn-on period, t_w the width, and $t_{\rm off}$ the time length for the electric field being present. In calculations, we take $t_c=75$ fs, $t_w=25$ fs, various values of electric field E_0, and the value of $t_{\rm off}$ is taken to be finite or infinite.

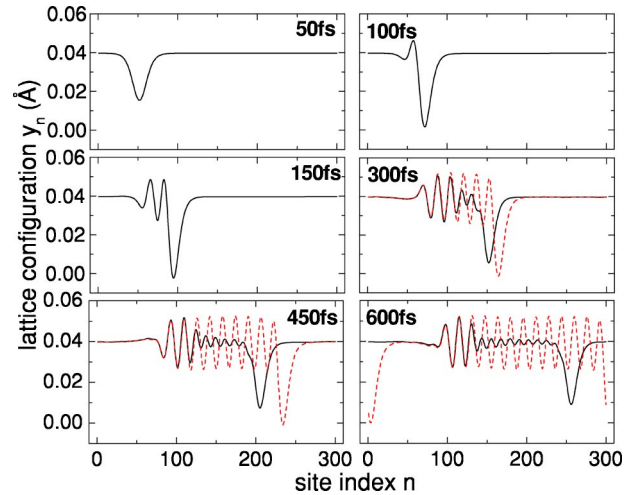

FIG. 1. Lattice configuration $\{y_n\}$ of the polaron motion under a moderate electric field ($E_0=3\times10^5$ V/cm) and $t_{\rm off}=150$ fs (solid lines) and $t_{\rm off}=\infty$ (dash lines).

III. RESULTS

In this section, we present our results on the phonon excitation in the motion of polaron in the presence of an external electric field. For that, we add one extra electron into the half-filled band of a ($N=300$) dimerized lattice (ring). We get the static polaron configuration by solving the self-consistent electron-lattice coupling Eqs. (4) and (5) with the N electrons doubly occupying the lowest $N/2$ electronic levels, the extra electron occupying the lowest $(N/2+1)$-th level. With the polaron (both the lattice configuration and the electron occupancy) as the initial condition, we will focus on the time evolution of the lattice configuration $\{y_n\}$, which is defined as

$$y_n = (-1)^n(2u_n-u_{n-1}-u_{n+1})/4.0, \tag{9}$$

through the solving of the Eqs. (6) and (7).

In Fig. 1, we show the time evolution of a polaron at a moderate electric field $E_0=3.0\times10^5$ V/cm and the time length for the field presence $t_{\rm off}=150$ fs. As a comparison, we also show in Fig. 1 the result for the field being kept (i.e., $t_{\rm off}=\infty$). From the figure, we can see clearly that due to the influence of the electric field, the polaron will move with a quite stable shape while the lattice oscillation behind the polaron is caused. A very interesting thing is that the lattice oscillation is induced only with the field being on. Once the field is shut off, while the polaron moves at a constant speed the lattice oscillation will not be induced and the previous induced lattice oscillation will be quite stable.

In order to show the difference of the polaron motion between the case when the field will be switched off and when the field is kept on, we define the charge center x_c as in Ref. 6

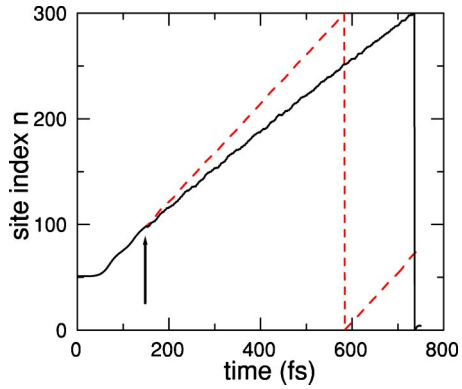

FIG. 2. The time evolution of the charge center x_c of the polaron under a moderate electric field ($E_0=3\times10^5$ V/cm) and $t_{\rm off}=150$ fs (solid line) and $t_{\rm off}=\infty$ (dash line). The arrow indicates the time at which the field was switched off (solid line).

$$x_c=\begin{cases} N\theta/2\pi, & \text{if } \langle\cos\theta_n\rangle\geqslant 0 \text{ and } \langle\sin\theta_n\rangle\geqslant 0;\\ N(\pi+\theta)/2\pi, & \text{if } \langle\cos\theta_n\rangle<0;\\ N(2\pi+\theta)/2\pi, & \text{otherwise,}\end{cases} \tag{10}$$

where

$$\theta=\arctan\frac{\sin\theta_n}{\cos\theta_n}, \tag{11}$$

and the average of $\sin\theta_n$ and $\cos\theta_n$ are defined as

$$\sin\theta_n=\sum_n\rho_n\sin\theta_n,\langle\cos\theta_n\rangle=\sum_n\rho_n\cos\theta_n, \tag{12}$$

with the probability weight $\rho_n(\equiv\rho_{n,n}-1)$ and $\theta_n=2\pi n/N$.

In Fig. 2, we show the time evolution of the charge center x_c of the polaron under a moderate electric field. From it, we can see that the polaron begins to move at about $t=75$ fs when the external field is increased to E_0 and the polaron gains enough energy. Then the polaron moves at a constant speed. At $t=150$ fs, the polaron will be shocked if the field is switched off. Then the polaron will move at a slightly slow speed as compared with that in the case where the field is kept on. This is easy to understand. In the case where the field is kept, the charge of the polaron will be forced ahead by the field and then it drags the lattice deformation of the polaron. It is clear that it is the drag that make a difference in the speed of the polaron motion. But in any case, the polaron will move at a constant speed for a very long time.

Now, we can understand why the polaron moves at a constant speed no matter if the field is switched off or not. When an electric field is applied, a charged polaron will reach a constant speed after being accelerated only for a short time, this is coincident with that obtained in Ref. 8. Since the electric field is present on the moving polaron, the energy of the system increases steadily. Then the moving polaron has to induce lattice oscillation behind itself since the polaron cannot move faster due to the lattice character. This is what we have seen in Fig. 1. Once the field is switched off, the energy of the system will not be changed, then the moving polaron does not need to emit phonons to keep its steady motion. While the polaron moves at a constant speed, the previous induced lattice oscillation moves at a slower speed, which we will see below, so that the lattice oscillation will be separated from the moving polaron and becomes quite localized and stable.

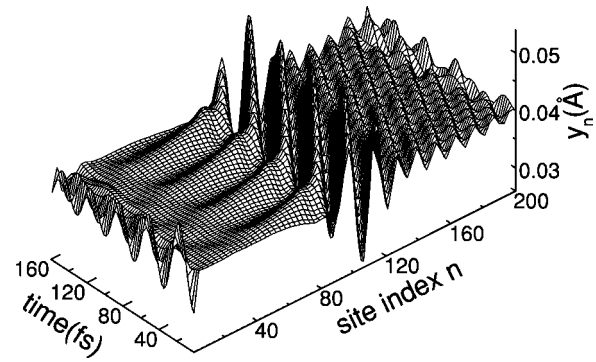

FIG. 3. Stereographic presentation of the n and t dependence of the lattice configuration $\{y_n\}$ in a ring of 200 sites. The initial ($t=0$) lattice configuration and velocities is copied from the lattice oscillation part induced by the moving polaron.

To clarify the characteristic properties of the lattice oscillation induced by the moving polaron, we separate the lattice oscillation from the moving polaron by copying the lattice configuration ($\{u_n(t)\}$) and site velocities ($\{\dot{u}_n(t)\}$) at $t=600$ fs excluding those at the 100 sites around the polaron into a ring of 200 sites. With the configuration and velocities as the initial condition, we do the simulation as done for the polaron motion but the electronic levels are filled only for the lower half part. The result is shown in Fig. 3, from which we can see clearly that the lattice oscillation exhibits the character of breathers, spatially localized, time periodic nonlinear excitations, and it shows to be quite stable for a very long time. The lattice oscillation period is about $T=40.8$ fs, which also coincides with that of breathers in the decay of an electron-hole pair into a soliton and antisoliton.[9,15]

As a comparison, let us see the temporal evolution of a breather in the discrete model (1) in the absence of external fields, that is the Su-Schrieffer-Heeger model.[2] We choose the lattice configuration as the initial condition for simulation by

$$u_n=(-1)^n u_0(1+\delta_n), \tag{13}$$

where u_0 is the dimerization magnitude, δ_n is given as[9,15]

$$\delta_n=\sqrt{6}\epsilon\,\mathrm{sech}(\sqrt{12}n\epsilon a/\xi_0)-\epsilon^2\,\mathrm{sech}^2(\sqrt{12}n\epsilon a/\xi_0), \tag{14}$$

where $\xi_0=t_0a/\alpha u_0$ and ϵ is the small expansion parameter which is related with the lattice oscillation period T.[9,15] In our case, $T=40.8$ fs, so $\epsilon=0.17$. The result is shown in Fig. 4, from which we can see the time evolution of a breather. By comparing what we have found in the motion of a polaron with the breather in Fig. 4, we know that is a multibreather state in Fig. 3. We show the lattice configuration $\{y_n\}$ of this multibreather state at various times in Fig. 5, from which we have (1) the lattice oscillation induced by a moving polaron is a state of breathers, which is a spatially

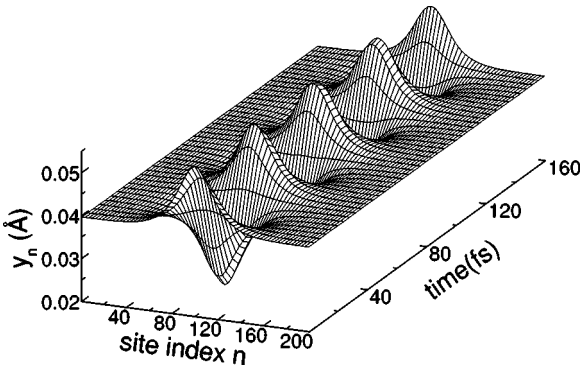

FIG. 4. Stereographic presentation of the n and t dependence of the lattice configuration $\{y_n\}$ in a ring of 200 sites. The initial ($t=0$) lattice configuration is given in Eq. (14).

localized, time periodic nonlinear excitation; (2) the nearest breathers have opposite phases; (3) the breathers have a small velocity [around $0.65v_s$, $v_s(\approx 1.53\times 10^6$ cm/s) the sound velocity], though its connection with the moving polaron has been cut; and (4) the breather is a bound state of phonons, due to the nonlinear interaction within phonons, there exists a tendency for extended phonons to get together for the form of breathers, so we can see that there are more breathers at $t=2400$ fs while those extended oscillation in front of the breathers fades away.

Finally we show in Fig. 6 the lattice configuration $\{y_n\}$ at around $t=600$ fs under an electric field of different strengths. Though the polaron velocity is slightly different for different electric fields, the number of induced breathers is the same. The amplitude and the distance between the nearest breathers depends on the strength of applied electric field. They are 0.007, 0.010, and 0.013 Å, and 7.0a, 7.5a, and 8.0a for the electric field $E_0=1.0\times 10^5$, $E_0=2.0\times 10^5$, and $E_0=3.0\times 10^5$ V/cm, respectively. Apparently, these breathers should have different energies since the strengths of the electric fields are different.

IV. DISCUSSION AND SUMMARY

As is well known, discrete breathers are periodic localized oscillations that arise in discrete nonlinear systems. The

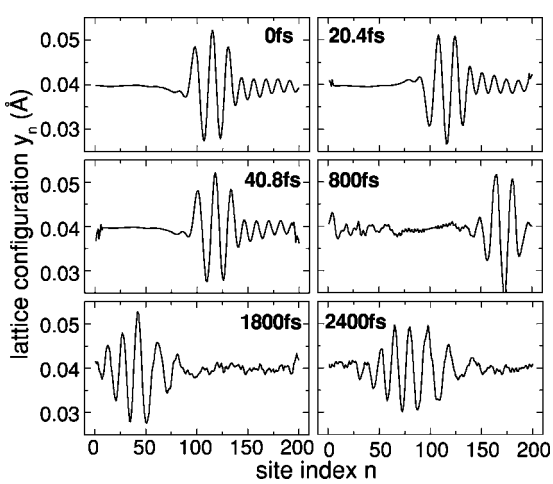

FIG. 5. Lattice configuration $\{y_n\}$ of the multibreather state at various times. All be the same as in Fig. 3.

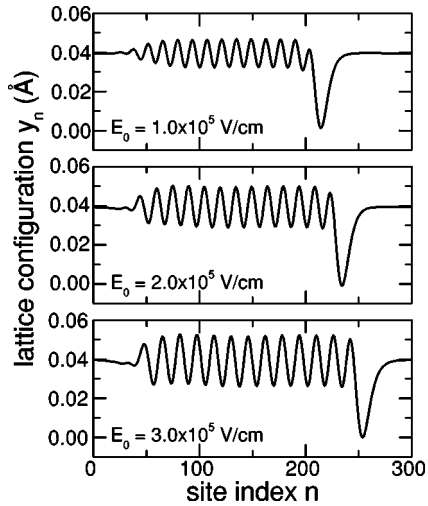

FIG. 6. Lattice configuration $\{y_n\}$ at around $t=600$ fs under an electric field of different strengths. All others are the same as in Fig. 1 ($t_{\rm off}=\infty$).

study on the breathers, in particular, the discrete breathers, has a long history.[12–14] While the static discrete breathers have been widely studied in nonlinear lattice systems since their existence was proven by MacKay and Aubry,[16] the mobility of discrete breathers is still an open issue due to the fact that moving discrete breathers are not solutions of the dynamical equations of the system that can be obtained using continuation methods and a proof of existence of them has not been found so far. In spite of that, there still are many numerical works on it. For example, by a systematic numerical method, Chen *et al.*[17] constructed mobile breathers through an appropriate perturbation of the pinning mode in discrete ϕ^4 nonlinear lattices and analyzed properties of breather motion and determined its effective mass. In addition, in a DNA model with competing short- and long-range dispersive interactions, mobile breathers are found to exist for a wide range of the parameter values, and the mobility of these breathers is found to be hindered by the long-range interaction.[18]

In conjugated polymers, which are modeled as electron-phonon interacting systems[2] and nonlinear interactions in the lattice come from the integration over the electrons, the breather was first found at the decay of an electron-hole pair into a soliton and antisoliton.[9,15] In the continuous version of the Su-Schrieffer-Heeger (SSH) model,[19] the analytic solution of a breather [see Eq. (14)] was obtained by a low-amplitude expansion,[9,15] and it has been shown to be a very accurate discrete breather in the discrete model of conjugated polymers, the SSH model, by both the adiabatic[9,15] and nonadiabatic (see Fig. 4) dynamical evolution methods. Very recently, the breather of a bound soliton pair in *trans*-polyacetylene has been realized by sub-five-femtosecond optical pulses.[20] A mobile multibreather excitation, what we found in this work, has not been reported before to the best of our knowledge not only in conjugated polymers but also in regular nonlinear lattice systems. A detailed investigation on it is underway.

Finally, one more interesting fact we should mention is that the breathers of significantly different amplitudes have

almost the same oscillation period ($T \approx 41$ fs), but the analytic solution of a nonlinear equation[9,15] indicates the amplitude is directly related with the oscillation period, which is actually a general property of a soliton. What does the phenomenon we found here imply? We are also waiting for the answer.

In summary, we have investigated the dynamical evolution of a polaron in a moderate-strength electric field. We found that the polaron under the influence of an external field has to emit phonons to keep its steady motion and these emitted phonons will be at a bound state, a moving multibreather state, which bears the increased energy of the system due to the action of the field. The nearest breathers have opposite phases. The number of induced breathers is the same for different electric fields at the same duration. The amplitude and the distance between nearest breathers depend on the applied electric field while the oscillation period is determined only by the electron-phonon coupling system.

ACKNOWLEDGMENTS

This work was partially supported by the National Natural Science Foundation of China (Grant Nos. 90103034, 10321003, and 10374017) and the State Ministry of Education of China (No. 20020246006). One of the authors (C.Q.W.) is grateful to the Institute of Materials Structure Science of KEK for the hospitality during his visit there.

*Corresponding author; electronic mail: cqw@fudan.edu.cn

[1] I. H. Campbell and D. L. Smith, Solid State Phys. **55**, 1 (2001) and references therein.
[2] W. P. Su, J. R. Schrieffer, and A. J. Heeger, Phys. Rev. Lett. **42**, 1698 (1979).
[3] S. A. Brazovskii and N. N. Kirova, Sov. Phys. JETP **33**, 4 (1981).
[4] A. J. Heeger, S. Kivelson, J. R. Schrieffer, and W. P. Su, Rev. Mod. Phys. **60**, 781 (1988).
[5] W. P. Su and J. R. Schrieffer, Proc. Natl. Acad. Sci. U.S.A. **77**, 1839 (1980).
[6] Y. Ono and A. Terai, J. Phys. Soc. Jpn. **59**, 2893 (1990).
[7] S. V. Rakhmanova and E. M. Conwell, Appl. Phys. Lett. **75**, 1518 (1999).
[8] A. Johansson and S. Stafström, Phys. Rev. Lett. **86**, 3602 (2001).
[9] A. R. Bishop, D. K. Campbell, P. S. Lomdahl, B. Horovitz, and S. R. Phillpot, Phys. Rev. Lett. **52**, 671 (1984); Synth. Met. **9**, 223 (1984).
[10] S. V. Rakhmanova and E. C. Conwell, Synth. Met. **110**, 37 (2000).
[11] C. Q. Wu, Y. Qiu, Z. An, and K. Nasu, Phys. Rev. B **68**, 125416 (2003).
[12] S. Flach and C. R. Willis, Phys. Rep. **295**, 181 (1998).
[13] A. J. Sievers and J. B. Page, in *Dynamical Properties of Solids VII. Phonon Physics*, edited by G. K. Horton and A. A. Maradudin (Elsevier, Amsterdam, 1995), p. 137.
[14] V. Fleurov, Chaos **13**, 676 (2003).
[15] S. R. Philpot, A. R. Bishop, and B. Horovitz, Phys. Rev. B **40**, 1839 (1989).
[16] R. S. MacKay and S. Aubry, Nonlinearity **7**, 1623 (1994).
[17] D. Chen, S. Aubry, and G. P. Tsironis, Phys. Rev. Lett. **77**, 4776 (1996).
[18] J. Cuevas, J. F. R. Archilla, Yu. B. Gaididei, and F. R. Romero, Physica D **163**, 106 (2002).
[19] H. Takayama, Y. R. Lin-Liu, and K. Maki, Phys. Rev. B **21**, 2388 (1980).
[20] S. Adachi, V. M. Kobryansckii, and T. Kobayashi, Phys. Rev. Lett. **89**, 027401 (2002).

Coexistence of localization and itineracy of electrons in boron-doped diamond

Jifeng Yu,[1] Kai Ji,[2] Changqin Wu,[3] and Keiichiro Nasu[1,2]
[1]*Department of Materials Structure Science, The Graduate University for Advanced Studies, CREST JST, 1-1 Oho, Tsukuba, Ibaraki 305-0801, Japan*
[2]*Solid State Theory Division, Institute of Materials Structure Science, KEK, 1-1 Oho, Tsukuba, Ibaraki 305-0801, Japan*
[3]*Department of Physics, Fudan University, Shanghai 200433, China*
(Received 18 July 2007; revised manuscript received 4 October 2007; published 16 January 2008)

In order to clarify the coexistence of a Fermi edge and the steplike multiphonon structure, recently observed in the photoemission spectra (PES) of the boron-doped diamond, we apply a path-integral theory to calculate the PES, using the many-impurity Holstein model in a simple cubic lattice. Being lightly doped by boron as an acceptor, the diamond shows *p*-type character with an activation energy gap of about 0.37 eV. We find that, due to the electron-phonon coupling and the increase of the dopant concentration, the impurity band extends up to the top of valence band, and fills the gap gradually. The emergence of a clear Fermi edge is theoretically demonstrated, indicating the strong itineracy of electrons from one impurity atom to another through those intermediate carbon atoms. Simultaneously, the multiphonon satellite structure, a little below the Fermi level, is also theoretically reproduced in the doped site PES, denoting the localization of electrons through the coupling with Einstein phonons. Although we have used a simpler lattice structure than the real diamond one, our exploration of the coexistence of the two intrinsic properties of electrons: itineracy and localization, well agrees with the experimental findings.

DOI: 10.1103/PhysRevB.77.045207 PACS number(s): 71.23.−k, 78.20.Bh, 79.60.−i

I. INTRODUCTION

The boron-doped diamond (BDD) has become one of the most investigated materials since the remarkable discovery of its superconductivity (SC).[1] So far, most researches have been focusing on the very nature of phonon exchange mechanism,[2–5] which is still unclear though agreed to be responsible for the SC. It is well known that the pristine diamond is an insulator with a wide band gap (about 5.5 eV). Being lightly doped with boron, it shows *p*-type character with an activation energy gap of about 0.37 eV.[6] Accompanied with the superconducting phase, a semiconductor-metal transition occurs when the doping percentage is increased to a certain level.[7,8] Recently, Ishizaka *et al.*[9] declared the observation of a steplike multiphonon satellite structure in the valence band photoemission spectra (PES), approximately distributed periodically at 0.150 eV below the Fermi level, in addition to the emergence of a clear Fermi edge, indicating the phase transition mentioned above on increasing the dopant concentration. Compared with the scanned Raman scattering spectrum, this side structure is supposed to be attributed to the strong electron-phonon (e-ph) coupling by these authors.[9] Giustino *et al.*[10] also suggested that the 0.150 eV phonon plays an important role in the SC by the first-principles technique on the e-ph interaction of this material.

Meanwhile, this periodic satellite structure reminds one of its similarity to that of a localized electron model,[11] wherein the coupling between electrons and Einstein phonons characterizes the spectrum with discrete peaks of equal energy interval. Thus, it is natural to infer that the e-ph coupling has a close relation to this steplike structure as well. More importantly, the Fermi edge and the steplike structure are observed together, probably originating from the two basic properties of electrons: itineracy and localization. It also should be noted that the multiphonon structure appears not in the well-known gap function of the SC, but in the PES of the normal state. Hence, it seems quite unusual that this coexistence is detected so clearly and directly. Because of this puzzling behavior as well as a probable connection with the SC, the problem how this coexistence occurs, thus, turns out to be a great challenge for the theorists.

The coherent potential approximation (CPA),[12] being a standard method dealing with disordered systems, however, has some limitation in explaining the emergence of the Fermi edge. Because this theory tacitly assumes that the system remains uniform even after the doping, thus it ensures the presence of a certain Fermi edge at the very beginning, even in the low doping cases, while the conventional treatments, such as Midgal-Eliashberg theory, usually invoke perturbation theories, and have difficulty in dealing with this disordered system.

In this study, we use a path-integral theory[13] to survey the PES of BDD system. Correspondingly, we adopt a many-impurity Holstein model based on a simple cubic lattice. Actually, the Holstein model[14] has been widely used to discuss the e-ph coupling problems in various cases. For example, Ref. 16 studied the evolution of the PES with momentum in the one-dimensional and two-dimensional pure systems, at half-filling or non-half-filling. Using a Monte Carlo simulation with the traveling cluster approximation, Ref. 17 has investigated the effect of disorder on electronic transport property in strong e-ph coupling systems of three dimensions. There are also discussions about the dynamics of a single electron in the Holstein model with[18] or without[19] disorder. In the present paper, we shall be concerned with the doping and the e-ph coupling effects on the PES, especially the quantum character of phonons seen in the PES, rather than the classical one discussed in Ref. 17. To evaluate the PES, we shall apply the path-integral theory to take into account all kinds of e-ph scattering processes, which is technically impossible for the conventional perturbative methods.

The main purpose of this work is to investigate the e-ph coupling effect on the PES of a many-electron system, and theoretically clarify the aforementioned coexistence, then interpret the experimental findings in BDD. Here, it should be stressed that we focus only on the energy region very close to the Fermi level. Hence, we can use a simple cubic lattice instead of the real diamond one to describe the various valence band features, with no attention to the region far from the Fermi level. Unlike the conventional approaches such as CPA, the "doping" in this work is a random substitution, according to a certain given doping rate, to describe the disordered situation in BDD. It should be noted that, in the present problem, the so-called randomness and the doped electron number are closely related and changed simultaneously, being different from both a simple randomness problem and a simple doping problem.

II. MODEL AND METHODS

As mentioned, our model includes the following two properties. One is the disorder of the system that some atoms are replaced by the dopant in a certain ratio. The other is the coupling between electrons and Einstein phonons (site-localized lattice vibration), being the simplest description of e-ph interactions, usually called Holstein model. Its Hamiltonian ($\equiv H$) is given as ($\hbar=1$ throughout the work),

$$H = -t\sum_{\langle l,l'\rangle}\sum_{\sigma}(a_{l\sigma}^{\dagger}a_{l'\sigma}+a_{l'\sigma}^{\dagger}a_{l\sigma}) - \mu\sum_{l,\sigma}n_{l\sigma} + \Delta_e\sum_{l_0,\sigma}n_{l_0\sigma} + \frac{\omega_0}{2}\sum_{l}\left(-\frac{\partial^2}{\partial Q_l^2}+Q_l^2\right) - S\sum_{l,\sigma}Q_l(n_{l\sigma}-\bar{n}_l/2),$$

$$n_{l\sigma}\equiv a_{l\sigma}^{\dagger}a_{l\sigma}, \quad \sigma=\alpha \text{ or } \beta, \tag{1}$$

where t is the hopping energy, set at $t=0.42$ eV in the simulations to match the real diamond band width. $a_{l\sigma}^{\dagger}$ and $a_{l\sigma}$ are the creation and annihilation operators of an electron with spin σ at site l. The electrons can hop only between the nearest neighboring sites expressed by $\langle l,l'\rangle$. μ stands for the chemical potential of electrons, and Δ_e is the potential difference after and before the substitution at the doped sites labeled by l_0. This parameter determines the formation and the position of the impurity band, i.e., the activation gap. It is determined according to the experimental value of about 0.37 eV. Q_l is the dimensionless coordinate operator of the phonon at site l, with a frequency ω_0. S denotes the e-ph coupling constant. $\bar{n}_l$ is the average electron number at site l. To simplify the problem, we just consider the coupling at the doped sites hereafter, because in pure diamond, there is no evidence that the phonon satellite structure appears. It implies that the coupling becomes important just after the doping, as discussed in Refs. 5 and 15. The doped boron atoms will introduce a strong coupling between the localized vibrational modes and electrons at around the Fermi surface of the BDD. There is also an experimental confirmation of this favored coupling in Ref. 20.

By using the Trotter decoupling formula and inserting the phonon eigenstate $|x_{l_0}\rangle$ of the operator Q_{l_0} by $Q_{l_0}|x_{l_0}\rangle = x_{l_0}|x_{l_0}\rangle$, the Boltzmann operator can be written in a path-integral form as[13]

$$e^{-\theta H} \to \int \mathcal{D}x\left[T_+\exp\left(-\int_0^{\theta}d\tau[h(\tau,x) + \Omega(\tau,x)]\right)\prod_{l_0}[|x_{l_0}(\theta)\rangle\langle x_{l_0}(0)|]\right], \tag{2}$$

where $\theta\equiv 1/k_BT$, T is the temperature, and

$$h(\tau,x) \equiv -t\sum_{\langle l,l'\rangle}\sum_{\sigma}[a_{l\sigma}^{\dagger}(\tau)a_{l'\sigma}(\tau)+a_{l'\sigma}^{\dagger}(\tau)a_{l\sigma}(\tau)] - \mu\sum_{l,\sigma}n_{l\sigma}(\tau) + \sum_{l_0,\sigma}n_{l_0\sigma}(\tau)[\Delta_e + S^2\bar{n}_{l_0}/\omega_0 - Sx_{l_0}(\tau)], \tag{3}$$

$$\Omega(\tau,x) \equiv \sum_{l_0}\left[Sx_{l_0}(\tau)\bar{n}_{l_0} + \frac{1}{2\omega_0}\left(\frac{\partial x_{l_0}(\tau)}{\partial\tau}\right)^2 + \frac{1}{2}\omega_0 x_{l_0}^2(\tau)\right]. \tag{4}$$

We should note that the electronic operators $a_{l\sigma}(\tau)$, $n_{l\sigma}(\tau)$ have no real time dependence. The time argument τ only denotes the time ordering operated by T_+. While $x_{l_0}(\tau)$ is a time dependent c number. $\int\mathcal{D}x$ means the summation over all possible paths.

We define a time evolution matrix $\mathbf{R}(\tau,x)$ along a path x as

$$\mathbf{R}(\tau,x) \equiv T_+\exp\left(-\int_0^{\tau}d\tau'\mathbf{H}[\tau',x(\tau')]\right), \tag{5}$$

where

$$[\mathbf{H}(\tau,x)]_{jj'} \equiv \langle 0|a_j(\tau)h(\tau,x)a_{j'}^{\dagger}(\tau)|0\rangle. \tag{6}$$

j symbolically stands for site l and spin σ, and $|0\rangle$ means the true electron vacuum. The one-body Green's function of a given path x is defined as

$$G(j\tau,j'\tau',x) = -\operatorname{sign}(\tau-\tau')\langle T_+\vec{a}_j(\tau)\vec{a}_{j'}^{\dagger}(\tau')\rangle_x, \tag{7}$$

which can be derived as

$$G(j\tau,j'\tau',x) = \left[\mathbf{R}(\tau,x)\begin{pmatrix} -\dfrac{1}{1+\mathbf{R}(\theta,x)}, & \tau>\tau' \\ \dfrac{1}{1+\mathbf{R}^{-1}(\theta,x)}, & \tau<\tau' \end{pmatrix}\mathbf{R}(\tau',x)\right]_{jj'}. \tag{8}$$

In Eq. (7), the operator $\vec{a}_j(\tau)$ is the Heisenberg representation of a_j, and is really time dependent. After the path integral, the ordinary Green's function $[\equiv G(ll',\tau)]$ is obtained as

$$G(ll',\tau) = \int \mathcal{D}x e^{-\theta[\Phi(x)-\Phi]} G(l\tau,l'0,x). \tag{9}$$

Here, $\Phi(x)$ and Φ are the free energy along a given path x and the total free energy, respectively. This Green's function is site dependent obviously.

In the numerical calculation, the path integral of Eq. (9) is performed by the quantum Monte Carlo (QMC) simulation with a path updating method similar to Ref. 21, which is much more rapid and efficient than the standard Metropolis algorithm. To avoid numerical errors, we have employed a matrix factorization algorithm[22] with quad precision. Since the starting phonon configuration is generated randomly, it is necessary to take enough extra QMC sweeps to reach the system thermal equilibrium before measuring the electron number or the Green's function. Furthermore, in order to reduce the correlation between the consecutive measurements, we set an interval of adequate sweeps. In the QMC, the chemical potential μ is first determined by checking the electron number.

Because of the broken translational symmetry of this disordered system, we cannot use Fourier transformation to get the momentum dependent Green's functions or the Green's function corresponding to the total density of state (DOS) by a summation over the momenta. Nevertheless, we can make use of the invariance of representation transformation to sum up the one-body Green's function $G(ll',\tau)$ over sites as

$$G(\tau) = \frac{1}{N}\sum_{l} G(ll,\tau). \tag{10}$$

Then the spectral function $A(\omega)$ can be derived through the analytic continuation as

$$G(\tau) = -\int_{-\infty}^{+\infty} \frac{e^{-\tau\omega}}{1+e^{-\theta\omega}} A(\omega) d\omega, \tag{11}$$

which is carried out here by an iterative fitting method introduced in Ref. 16. Here, we should mention that in Eq. (10), N can be either the total system size or a part of it, such as all the doped sites, depending on the site l we choose. That is to say, we can calculate different spectra by selecting different l, which will be shown and discussed in detail later. Finally, the PES intensity function $I(\omega)$ is calculated as $I(\omega) = A(\omega)f(\omega)$ by imposing the Fermi distribution $f(\omega)$ to compare with the experimental results, since the PES experiment only detects the occupied electronic states.

III. RESULTS AND DISCUSSIONS

Because we take into account the e-ph coupling only at those doped sites, the phonon effect is not so clear in the whole system spectrum after averaging over all sites. To clarify the phonon quantum effect, we shall also present the spectral intensity of doped sites.

First, as a reference, we compute the spectra for the simple cubic lattice of different doping rates by the classical Monte Carlo (CMC) simulation[23] as shown in Fig. 1, wherein the kinetic energy of the phonon is neglected and the one-body Green's function is obtained by directly diagonalizing the electronic Hamiltonian. The system size is $8\times8\times8$, and the parameters are $\omega_0=0.25$ eV, $S=0.25$ eV, and $\theta=14.4$ eV^{-1}. Correspondingly, the dimensionless coupling constant λ ($\equiv\frac{S^2}{2d\omega_0 t}$, where d is the dimension) is 0.1. From the whole system spectra (solid lines), we can clearly see the emergence of a Fermi edge on increasing the doping percentage. In the low doping case, the impurity levels are a little above the top of the valence band, and the material is a semiconductor with a small activation gap. In the higher doping case, the impurity band expands up to the top of the valence band, and the gap is filled up. Thus, the sample undergoes a semiconductor-metal transition, and the electrons can move freely from one impurity atom to another by tunneling through the intermediate carbon atoms. As for the spectra of doped sites (dashed lines), apart from the main impurity band, there is a long tail extending almost over the valence band. This is due to the modification of impurity levels by an admixture of the continuum valence band, as described by the Fano effect.[24] This effect is also exhibited in Ref. 22 by using a static single-impurity model to explain the origin of the multipeak spectra.

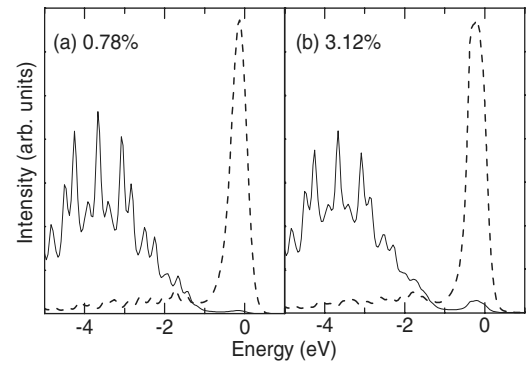

FIG. 1. The spectra for the simple cubic lattice of different doping rates by the QMC. The zero is the position of the Fermi level. Dotted lines and solid ones denote the spectra of doped sites and the whole system, respectively.

In Fig. 2, we calculate the spectra for the simple cubic lattice of different doping rates by the QMC method, which is free from the approximation used in the previous CMC. The parameters are the same as in Fig. 1. Since the system size is small, $4\times4\times4$, the value of the doping rate seems to be relatively high, but the absolute number of the doped sites is small. In the whole system spectra (solid lines), the semiconductor-metal phase transition is reproduced completely with the increase of doping rate. In order to illustrate the different contributions to the DOS from doped atoms and undoped atoms, the undoped site spectrum (dashed line) and the whole system spectrum (solid line) near the Fermi level are shown as an inset in Fig. 2(c). It is obvious that the disordered states in the PES make the activation gap smaller.

In Fig. 2, for the doped site spectra (dashed lines), a phonon satellite structure is clearly seen in each panel, lying a little below the Fermi level, in addition to the aforementioned Fano tail. This side structure has not been found in the classical cases, and obviously comes from the phonon quantum property in the e-ph coupling, while its shape is should-

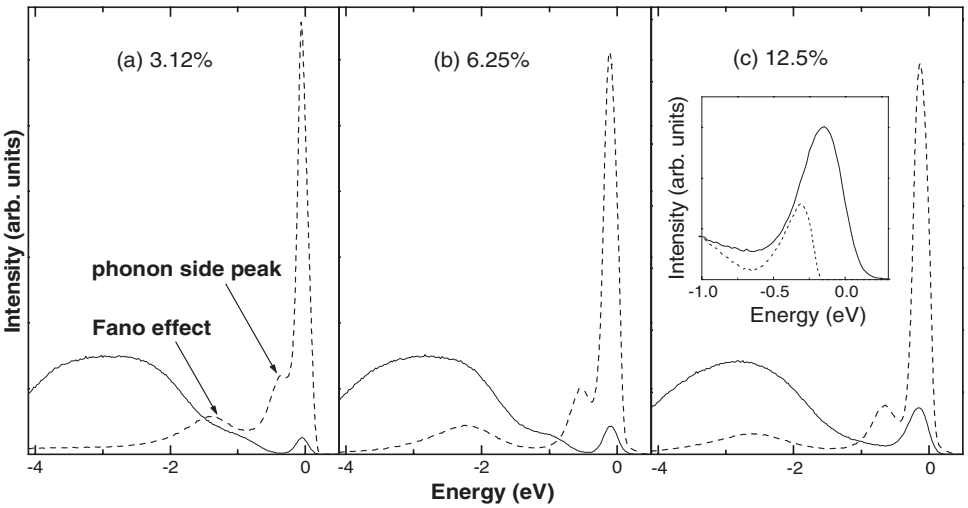

FIG. 2. The spectra for the simple cubic lattice of different doping rates by the QMC. The zero is the position of the Fermi level. Dotted lines and solid ones denote the spectra of doped sites and the whole system, respectively. The inset in (c) is the whole system spectrum (solid curve) and the undoped site spectrum (dashed curve) near the Fermi level.

erlike instead of the δ-function-like peaks given in the localized electron model.[11] Actually, in our QMC simulations, we have used several different values of phonon frequency between 0.10 and 0.30 eV. The phonon structures are observed in all these cases, but most clearly when $\omega_0 \geqslant 0.25$ eV, due to low resolution and temperature limitation of the QMC approach. Although we show only the results of $\omega_0=0.25$ eV here, we believe the physical essence of the steplike satellite structure is already captured through this calculation.

We should note that in the three panels of Fig. 2, the positions of the phonon side peaks (dashed lines), 0.3 eV in (a), 0.5 eV in (b), and 0.6 eV in (c), are a little different from the ones expected from the phonon frequency we have used ($\omega_0=0.25$ eV). As discussed in Refs. 16 and 25, the PES of a uniform system is determined by the simultaneous momentum and energy conservation of the e-ph system. The energy interval ($\equiv\Delta\varepsilon$) between the zero-phonon (no e-ph scattering) peak and the single-phonon one is dependent not only on the phonon frequency but also on the electron energy band by the formula $\Delta\varepsilon=(\varepsilon_{p+q}+\omega_{-q})-\varepsilon_p$, where ε_p denotes the energy of an original photoemitted electron with momentum p. It changes to $\varepsilon_{p+q}+\omega_{-q}$ after emitting a phonon of momentum $-q$. The localized electron model is a special case, wherein the electron is pinned at one site. Thus, the self-scattering process guarantees that the interval is decided only by the phonon frequency. Using Einstein phonons, it is naturally of an equal interval. As for the present model, it bears similarities to the above two cases, as denoted in the Hamiltonian. In the low doping rate case such as Fig. 2(a), the impurity levels are few or the impurity band is very shallow, which is similar to the localized electron case, then the interval between the zero-phonon peak and the single-phonon peak is almost equal to the Einstein phonon frequency. In heavily doped samples such as shown in Figs. 2(b) and 2(c), the impurity band expands and its shape plays greater roles, then the side structure appears to be much wider and irregular in position. At the same time, this single-phonon peak is also modified by the impurity band to shift a little from the original position of 0.25 eV and become asymmetric according to the aforementioned Fano effect. When combined together, it presents as a shoulderlike shape in the doped site spectra, with irregular energy intervals, even within the Einstein phonon model.

Obviously, the e-ph coupling also greatly contributes to the expansion of the impurity band and the filling of the activation gap. As shown in Fig. 2, the phonon side structure lies a little below the Fermi level, at the very scope of the semiconductor gap. If the e-ph effect is strong or the doping rate is high, this side structure expansion in the doped site spectra can contribute much to the whole system spectra. In Fig. 3, we give the spectra of a low doping rate, same as Fig. 2(a), but increasing the coupling constant to 0.5 eV instead of $S=0.25$ eV used in Figs. 1 and 2. Then, the λ is 0.4. Comparing with Fig. 2(a), the strong coupling between the electrons and the phonons not only greatly intensifies the single-phonon peak, but also arouses double-phonon or even multiphonon scattering processes, because another shoulder appears clearly besides the investigated single-phonon one and the Fano tail in the doped sites spectrum (dashed line). Thus, the localization character of electrons is exhibited incisively and vividly. As discussed above, this effect can expand the impurity band to fill the gap, thus making the phase transition occur, as shown clearly in the whole system spec-

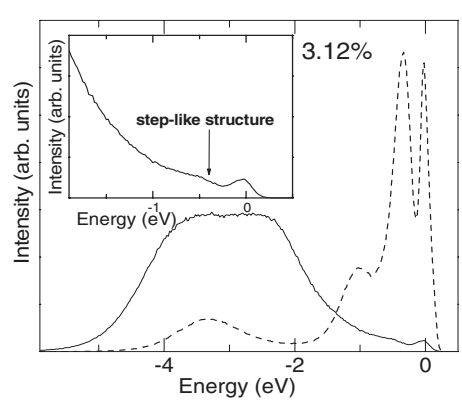

FIG. 3. The spectra for doped simple cubic lattice with an intermediate e-ph coupling. The zero is the position of the Fermi level. The dotted (solid) line is the spectrum of doped sites (the whole system). The inset is a zoom in on the solid line near the Fermi level.

trum (solid line). Though obscure, we can even affirm the steplike shape in the whole system spectrum, which locates at the very position of the single-phonon peak in the doped site spectra. The region near the Fermi level is zoomed in at the inset. From this figure, we can see clearly the coexistence of a Fermi edge and the steplike multiphonon satellite structure.

The multiphonon process can be clearly seen only in the larger S case. While in the small S case, only the single-phonon process can be observed. So, we just pick two typical S cases (weak one and intermediate one) for this paper. They are enough to clarify the physics and the experiment.

As mentioned, the path-integral theory we used here has one more advantage over the CPA. It can distinguish the different components in the material as we have done in calculating the spectra of doped and undoped sites. In reality, this differentiation can be achieved by the resonance PES[25] experiments. Tuning the incident photon energy to stimulate the atom core-level absorption excitation, the possible immediate Auger decay emits an electron, which can interfere with a directly photoemitted valence band electron. The overlap of these two electrons can be described as a function of the incident photon energy by the so-called Fano line shape.[24] For the material BDD, the excitation energy of carbon core-level 1S to the top of the valence band is about 284 eV, much different from that of boron, which is about 190 eV. Therefore, by sweeping the photon energy from low values through the above values, the spectrum reflecting the boron atom core-level absorption can be observed first, and then the carbon atoms; thus, the different components are identified.

IV. CONCLUSION

In summary, we have calculated the PES of the doped simple cubic lattice by applying a path-integral theory to the many-impurity Holstein model to reproduce the coexistence of a Fermi edge and the multiphonon satellite structure, which embodies the coexistence of the two intrinsic attributes of electrons: itineracy and localization. The one-body lattice Green's function is calculated by the QMC method to derive the spectral function. Due to the e-ph coupling and the increase of dopant concentration, the impurity band extends up to the top of the valence band, and then fills the semiconductor gap gradually. The semiconductor-metal transition takes place. Thus, the electrons can itinerate from one impurity atom to another one through those intermediate carbon atoms. At the same time, the coupling between electrons and Einstein phonons induces the multiphonon steplike satellite structure, indicating the localization of the electrons by Einstein phonons. Though using a simple lattice structure, our theoretical interpretation is quite important to clarify the coexistence of a Fermi edge and the steplike satellite structure detected in the PES of the BDD. Since silicon has a similar lattice structure to diamond, and the doping with boron is also substitutional,[26] these characteristics are also expected in boron-doped silicon, in which the SC is discovered recently.[26]

ACKNOWLEDGMENT

This work was supported by the next generation of supercomputing project, Nanoscience program, MEXT, Japan.

[1] E. A. Ekimov, V. A. Sidorov, E. D. Bauer, N. N. Mel'nik, N. J. Curro, J. D. Thompson, and S. M. Stishov, Nature (London) **428**, 542 (2004).
[2] L. Boeri, J. Kortus, and O. K. Andersen, Phys. Rev. Lett. **93**, 237002 (2004).
[3] K. W. Lee and W. E. Pickett, Phys. Rev. Lett. **93**, 237003 (2004).
[4] Y. Ma, J. S. Tse, T. Cui, D. D. Klug, L. Zhang, Y. Xie, Y. Niu, and G. Zou, Phys. Rev. B **72**, 014306 (2005).
[5] X. Blase, Ch. Adessi, and D. Connétable, Phys. Rev. Lett. **93**, 237004 (2004).
[6] A. T. Collins and A. W. S. Williams, J. Phys. C **4**, 1789 (1971).
[7] E. Bustarret, J. Kačmarčik, C. Marcenat, E. Gheeraert, C. Cytermann, J. Marcus, and T. Klein, Phys. Rev. Lett. **93**, 237005 (2004).
[8] Y. Takano, M. Nagao, T. Takenouchi, H. Umezawa, I. Sakaguchi, M. Tachiki, and H. Kawarada, Diamond Relat. Mater. **14**, 1936 (2005).
[9] K. Ishizaka, R. Eguchi, S. Tsuda, T. Kiss, T. Shimojima, T. Yokoya, S. Shin, T. Togashi, S. Watanabe, C.-T. Chen, C. Q. Zhang, Y. Takano, M. Nagao, I. Sakaguchi, T. Takenouchi, and H. Kawarada, Sci. Technol. Adv. Mater. **7**, S17 (2006).
[10] F. Giustino, J. R. Yates, I. Souza, M. L. Cohen, and G. Louie, Phys. Rev. Lett. **98**, 047005 (2007).
[11] G. D. Mahan, *Many-Particle Physics*, 3rd ed. (Plenum, New York, 2000), Chap. 4.
[12] P. Soven, Phys. Rev. **156**, 809 (1967).
[13] K. Nasu, J. Phys. Soc. Jpn. **65**, 2285 (1996).
[14] T. Holstein, Ann. Phys. (N.Y.) **8**, 325 (1959).
[15] H. J. Xiang, Z. Li, J. Yang, J. G. Hou, and Q. Zhu, Phys. Rev. B **70**, 212504 (2004).
[16] K. Ji, H. Zheng, and K. Nasu, Phys. Rev. B **70**, 085110 (2004).
[17] S. Kumar and P. Majumdar, Phys. Rev. Lett. **94**, 136601 (2005).
[18] F. X. Bronold, A. Saxena, and A. R. Bishop, Phys. Rev. B **63**, 235109 (2001).
[19] S. Ciuchi, F. de Pasquale, S. Fratini, and D. Feinberg, Phys. Rev. B **56**, 4494 (1997).
[20] M. Ortolani, S. Lupi, L. Baldassarre, U. Schade, P. Calvani, Y. Takano, M. Nagao, T. Takenouchi, and H. Kawarada, Phys. Rev. Lett. **97**, 097002 (2006).
[21] R. Blankenbecler, D. J. Scalapino, and R. L. Sugar, Phys. Rev. D **24**, 2278 (1981).
[22] M. Yamazaki, N. Tomita, and K. Nasu, J. Phys. Soc. Jpn. **72**, 611 (2003).
[23] J. Han, K. Ji, Z. Zhu, and K. Nasu, Phys. Rev. B **73**, 125111 (2006).
[24] U. Fano, Phys. Rev. **124**, 1866 (1961).
[25] F. Reinert and S. Hüfner, New J. Phys. **7**, 97 (2005).
[26] E. Bustarret, C. Marcenat, P. Achatz, J. Kačmarčik, F. Lévy, A. Huxley, L. Ortéga, E. Bourgeois, X. Blase, D. Débarre, and J. Boulmer, Nature (London) **444**, 465 (2006).

Novel theoretical approach in photoemission spectroscopy: application to isotope effect and boron-doped diamond

J Yu, K Ji and K Nasu

CREST JST, Solid State Theory Division, Institute of Materials Structure Science, KEK, Graduate University for Advanced Studies, Oho 1-1, Tsukuba, Ibaraki 305-0801, Japan

E-mail: jikai@post.kek.jp

Abstract. A new path-integral theory is developed to calculate the photoemission spectra (PES) of correlated many-electron systems. The application to the study on $Bi_2Sr_2CaCu_2O_8$ (Bi2212) and boron-doped diamond (BDD) is discussed in details. It is found that the isotopic shift in the angle-resolved photoemission spectra of Bi2212 is due to the off-diagonal quadratic electron-phonon (e-ph) coupling, whereas the presence of electron-electron repulsion partially suppresses this effect. For the BDD, a semiconductor-metal phase transition, which is induced by increasing the e-ph coupling and dopant concentration, is reproduced by our theory. Additionally, the presence of Fermi edge and phonon step-like structure in PES is found to be due to a co-existence of itinerant and localized electronic states in BDD.

1. Introduction

The role of electron-phonon (e-ph) interaction in the high-T_c superconductivity has received considerable attention since the discovery of oxygen isotope effect of $Bi_2Sr_2CaCu_2O_8$ (Bi2212) in the angle-resolved photoemission spectra (ARPES)[1, 2]. The experimental data show that electronic band is shifted slightly with the $^{16}O/^{18}O$ substitution, signifying the existence of e-ph interplay in cuprates. Besides, theoretically clarifying this effect is of great significance, for the energy scale of shifts reported by the two groups in Refs. [1] and [2] seem quite inconsistent with each other, and many questions still remain up to now. In order to have an insight into the isotope effect, in this work, we develop a new path-integral theory to calculate the photoemission spectra (PES) of cuprate superconductors, in which the electron-electron (e-e) and e-ph correlations are treated on an equal footing. This theory is also applicable to other kind correlated materials. As an example, here, we also study the PES of boron-doped diamond (BDD), which undertakes a semiconductor-metal phase transition on doping, and becomes a superconductor with the temperature decreases[3]. The details of our theory will be presented in the next section, in connection with the study on isotope effect. Calculation and discussion on PES of BDD are included in Section 3. A concluding remark can be found in the Summary.

2. Isotopic shift in ARPES of $Bi_2Sr_2CaCu_2O_8$

2.1. Model for CuO_2 plane of cuprate superconductor

In the CuO_2 plane of cuprates, the electronic transfer is modulated by the vibration of oxygen atoms between the initial and final Cu sites (see in Fig. 1), resulting in an off-diagonal type

e-ph coupling. In order to qualitatively clarify the isotope effect of Bi2212, we start from a half-filled Hamiltonian including the e-e repulsion and the above mentioned off-diagonal e-ph coupling ($\hbar = 1$ and $k_B = 1$ throughout this paper):

$$H = -\sum_{\langle l,l'\rangle,\sigma} t(l,l')(a^\dagger_{l\sigma}a_{l'\sigma} + a^\dagger_{l'\sigma}a_{l\sigma}) + U\sum_l n_{l\uparrow}n_{l\downarrow} + \frac{\omega_0}{2}\sum_{\langle l,l'\rangle}\left(-\frac{1}{\lambda}\frac{\partial^2}{\partial q^2_{ll'}} + q^2_{ll'}\right), \quad (1)$$

where $a^\dagger_{l\sigma}$ ($a_{l\sigma}$) is the creation (annihilation) operator of an electron with spin σ at the Cu site l on a square lattice (Fig. 1). The electrons hop between two nearest neighboring Cu sites, denoted by $\langle l,l'\rangle$, with a transfer energy $t(l,l')$. U is the strength of Coulomb repulsion between two electrons on the same Cu site with opposite spins. The oxygen phonon is assumed to be of the Einstein type with a frequency ω_0 and a mass m. λ ($\equiv 1+\Delta m/m$) is the mass change factor of phonon due to the isotope substitution. In the third term, $q_{ll'}$ is the dimensionless coordinate operator of the oxygen phonon locating between the nearest-neighboring Cu sites l and l', and the sum denoted by $\langle l,l'\rangle$ just means a summation over all the phonon sites in the lattice.

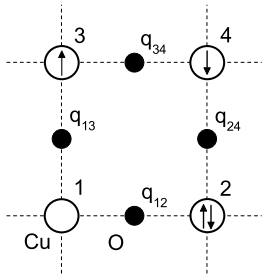

Figure 1. Lattice structure of CuO_2 conduction plane in cuprates. The copper atom (white circle) is on the l-th site of a simple square lattice, where the electrons (arrows) reside. The oxygen atom (black circle) is located between the nearest-neighboring Cu sites, and $q_{ll'}$ denotes its displacement from the equilibrium position.

In the conduction plane of CuO_2, the electronic hopping integral $t(l,l')$ can be expanded to the second order terms with respect to the phonon displacements $q_{ll'}$ as

$$t(l,l') = t_0 + sq^2_{ll'}, \quad (2)$$

where t_0 is the bare hopping energy and s the off-diagonal quadratic e-ph coupling constant. Here we note the linear e-ph coupling does not occur owing to the lattice symmetry of present model. Whereas the inter-site e-e interaction is included in the screened values of t_0 and s.

2.2. Path-integral Monte Carlo method

In this section, we develop a path-integral theory for a model with both e-e and e-ph interactions. By making use of the Trotter's decoupling formula, the Boltzmann operator is written as,

$$e^{-\beta H} = \lim_{L\to\infty}\left(e^{-\Delta H}\cdots e^{-\Delta H}\right). \quad (3)$$

Applying the Hubbard-Stratonovitch transformation[4] and the Gaussian integral formula[5], we can decouple the two-body parts, so that the e-e and e-ph correlated terms are replaced by a two-fold summation over the auxiliary spin and lattice configurations, which is the so-called path-integral. In this way, the Boltzmann operator is rewritten into the path-integral form as,

$$e^{-\beta H} \rightarrow \int \mathcal{D}x\left(T_+\exp\left\{-\int_0^\beta d\tau\,[h(\tau,x_m,x_q)+\Omega(x_q)]\right\}\prod_l\left[|x_q(l,\beta)\rangle\langle x_q(l,0)|\right]\right), \quad (4)$$

$$
\begin{aligned}
h(\tau, x_m, x_q) &\equiv -\sum_{\langle l,l'\rangle,\sigma} \left[t_0 + s x_q^2(l,l',\tau)\right] \left[a_{l\sigma}^\dagger(\tau) a_{l'\sigma}(\tau) + a_{l'\sigma}^\dagger(\tau) a_{l\sigma}(\tau)\right] \\
&\quad -\sqrt{\frac{U}{\Delta}} \sum_l x_m(l,\tau)[n_{l\uparrow}(\tau) - n_{l\downarrow}(\tau)], \qquad (5) \\
\Omega(x_q) &\equiv \sum_{\langle l,l'\rangle} \left\{ \frac{\lambda}{2\omega_0} \left[\frac{\partial x_q(l,l',\tau)}{\partial \tau}\right]^2 + \frac{1}{2}\omega_0 x_q^2(l,l',\tau) \right\}. \qquad (6)
\end{aligned}
$$

Here, x_m and x_q correspond to the auxiliary spin and lattice field, respectively, $\int \mathcal{D}x$ symbolically denotes the integrals over the path x synthesized by x_m and x_q, and $|x_q\rangle$ is the eigenstate of phonon. Δ is the time interval of the Trotter's formula, $\beta \equiv 1/T$, and T is the absolute temperature. T_+ in Eq. (4) is the time ordering operator.

Then the time evolution operator $[\equiv R(\tau, x)]$ along a path x is defined as

$$
R(\tau, x) = T_+ \exp\left[-\int_0^\tau d\tau' h(\tau', x_m, x_q)\right]. \qquad (7)
$$

In terms of the Boltzmann operator (4) and time evolution operator (7), we define the free energy $[\equiv \Phi(x)]$ of the given path as

$$
e^{-\beta\Phi(x)} = e^{-\int_0^\beta d\tau \Omega(x_q)} \mathrm{Tr}\left[R(\beta, x)\right]. \qquad (8)
$$

While, the partition function ($\equiv Z$) and total free energy ($\equiv \Phi$) are given as

$$
Z = e^{-\beta\Phi} = \int \mathcal{D}x e^{-\beta\Phi(x)}. \qquad (9)
$$

According to Refs. [4] and [5], we also define the one-body Green's function $[\equiv G_\sigma(l\tau, l'\tau', x)]$ on a path x as

$$
G_\sigma(l\tau, l'\tau', x) = -\mathrm{sign}(\tau - \tau')\langle T_+ \vec{a}_{l\sigma}(\tau) \vec{a}_{l'\sigma}^\dagger(\tau')\rangle_x, \qquad (10)
$$

where $\vec{a}_{l\sigma}(\tau)$ is the Heisenberg representation of $a_{l\sigma}$. It is really time-dependent and defined by

$$
\vec{a}_{l\sigma}(\tau) \equiv R^{-1}(\tau, x) a_{l\sigma} R(\tau, x). \qquad (11)
$$

Meanwhile, the ordinary Green's function $[\equiv G_\sigma(l, \tau)]$ can be obtained by the path-integral as

$$
G_\sigma(l - l', \tau - \tau') = \frac{1}{Z} \int \mathcal{D}x e^{-\beta\Phi(x)} G_\sigma(l\tau, l'\tau', x). \qquad (12)
$$

This path-integral is evaluated by the quantum Monte Carlo (QMC) simulation method.

If the QMC data of Green's function $G_\sigma(l, \tau)$ is obtained, we can immediately calculate its Fourier component $[\equiv G_\sigma(\mathbf{k}, \tau)]$ as

$$
G_\sigma(\mathbf{k}, \tau) = \frac{1}{N} \sum_l G_\sigma(l, \tau) e^{-i\mathbf{k}\cdot\mathbf{R}_l}, \qquad (13)
$$

where $\mathbf{k}$ is the momentum of the outgoing photo-electron. From this Fourier component $G_\sigma(\mathbf{k}, \tau)$, we derive the momentum-specified spectral function $[\equiv A_\sigma(\mathbf{k}, \omega)]$ by solving the integral equation

$$
G_\sigma(\mathbf{k}, \tau) = -\int_{-\infty}^{\infty} d\omega \frac{e^{-\tau\omega}}{1 + e^{-\beta\omega}} A_\sigma(\mathbf{k}, \omega). \qquad (14)
$$

2.3. Isotope substitution induced band shift in ARPES

We now present the QMC results on a 4×4 square lattice, where t_0 is set as the unit of energy, and ω_0=1.0 is used. For the QMC simulation, we impose a little large isotopic mass enhancement, λ_0=1 and λ=2, to suppress the numerical error. In this calculation, we determine the binding energy $\epsilon_{\mathbf{k}}$ by the moment analysis of the spectral function as $\epsilon_{\mathbf{k}} = \sum_\sigma \int d\omega A_\sigma(\mathbf{k},\omega)\omega$. Correspondingly, the isotope induced band shift is calculated by $\Delta\epsilon_{\mathbf{k}} \equiv \epsilon_{\mathbf{k}}(\lambda) - \epsilon_{\mathbf{k}}(\lambda_0)$.

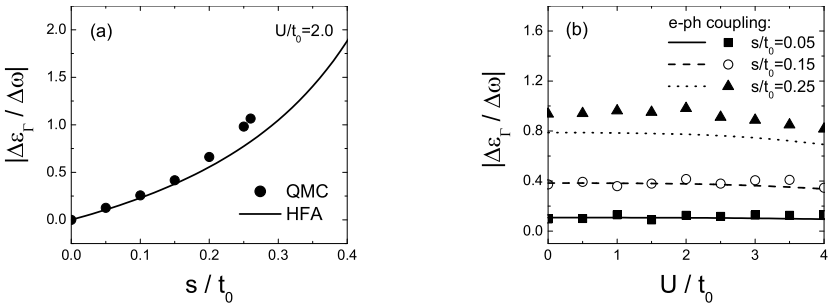

Figure 2. (a) The variation of $\Delta\epsilon_\Gamma/\Delta\omega$ with s on a 4×4 square lattice, when U=2.0, β=10, λ_0=1, λ=2. The filled circles are from QMC, and the solid curve from HFA as a guide for eyes. (b) The variations of $\Delta\epsilon_\Gamma/\Delta\omega$ with U on a 4×4 square lattice at β=10, λ_0=1 and λ=2. Three different values of s are used to show the s-dependence of $\Delta\epsilon_\Gamma/\Delta\omega$. The discrete symbols are the results of QMC, and continuous curves by HFA as a reference.

In Fig. 2(a), we plot the ratio $\Delta\epsilon_\Gamma/\Delta\omega$ versus s, at U=2.0 and β=10, where $\Delta\epsilon_\Gamma$ is the band shift at the Γ point of Brillouin zone [$\mathbf{k}_\Gamma$=(0,0)], and $\Delta\omega$ is the isotopic change of phonon energy. The filled circles are calculated by QMC, and the solid curve by the mean-field theory with Hartree-Fork approximation (HFA) as a guide for eyes. Here both theories figure out an increase of $\Delta\epsilon_\Gamma/\Delta\omega$ with s, which means if the e-ph coupling is strong enough, a large band shift can be generated in a small cost of $\Delta\omega$. In Fig. 2(b), the ratio $\Delta\epsilon_\Gamma/\Delta\omega$ versus U are shown for three different s's, where the discrete symbols and continuous curves are the QMC and HFA results, respectively. One can see the ratio $\Delta\epsilon_\Gamma/\Delta\omega$ increases with s. Meanwhile, for a fixed s, the ratio declines slightly as U increases, indicating that the band shift is owing to the e-ph coupling, whereas the presence of U partially reduces this effect. According to Fig. 2, the band shift thus can be regarded as a measure of the effective e-ph coupling strength in the system.

3. Co-existence of localization and itineracy of electrons in boron-doped diamond

It is well known that the pristine diamond is a big band gap insulator. Lightly doped with boron, it shows a p-type character with an activation energy about 0.37 eV[6]. Recently, the research on BDD has become highly attractive since the remarkable discovery of superconductivity in this material[3]. Accompanied with the superconducting phase, a semiconductor-metal transition also occurs when the doping percentage is increased to certain level. In the normal metallic state, K. Ishizaka *et al.*[7] declared the observation of a step-like multi-phonon satellite structure in the valence band PES, approximately distributed periodically in 0.150 eV below the Fermi level, in addition to the emergence of a clear Fermi edge. This periodic structure in PES reminds us of a similarity to the case of localized electron[8], wherein the coupling between electron and Einstein phonons characterizes the spectra with discrete peaks at equal distance. Moreover, the Fermi edge and the step-like structure are observed together, probably originating from a co-existence of the two basic properties of electrons: itineracy and localization. In order to clarify this so-called co-existence theoretically, we apply our path-integral theory to the many-impurity-Holstein (MIH) model on a doped simple cubic lattice to derive its spectral density.

3.1. Model and methods

The MIH model includes the following two properties. One is the disorder of the system, that some atoms are replaced by dopant ones in a certain ratio. The other is the coupling between electrons and Einstein phonons, being the simplest description of e-ph interactions. Its Hamiltonian is given as,

$$\begin{aligned} H &= -t\sum_{\langle l,l'\rangle}\sum_{\sigma}(a^{\dagger}_{l\sigma}a_{l'\sigma}+a^{\dagger}_{l'\sigma}a_{l\sigma})-\mu\sum_{l,\sigma}n_{l\sigma}+\Delta_e\sum_{l_0,\sigma}n_{l_0\sigma}+\frac{\omega_0}{2}\sum_{l}\left(-\frac{\partial^2}{\partial Q_l^2}+Q_l^2\right) \\ &\quad -S\sum_{l,\sigma}Q_l(n_{l\sigma}-\overline{n}_l/2), \quad n_{l\sigma}\equiv a^{\dagger}_{l\sigma}a_{l\sigma},\ \sigma=\alpha \text{ or } \beta, \end{aligned} \tag{15}$$

where t is the transfer energy. $a^{\dagger}_{l\sigma}$ and $a_{l\sigma}$ are the creation and annihilation operators of electron with spin σ at site l. Electrons can hop only between the nearest neighboring sites expressed by $\langle l,l'\rangle$. μ stands for the chemical potential of electrons and Δ_e is the potential difference between after and before substitution at the doped sites labeled by l_0. Q_l is the dimensionless coordinate operator for the phonon at site l with frequency ω_0. S denotes the e-ph coupling constant. $\overline{n}_l$ is the average electron number at site l. To simplify the problem, we just consider the coupling at the doped sites hereafter, because in the pure diamond there is no evidence that the satellite structure appears, which suggests the coupling is important only after doping.

By applying our path-integral theory to the disordered system, and following the formulation in Section 2.2, we obtain an electronic Green's function similar to Eq. 12,

$$G_\sigma(l,\tau)=\frac{1}{Z}\int\mathcal{D}x e^{-\beta\Phi(x)}G_\sigma(l\tau,l0,x). \tag{16}$$

In the numerical calculation, the path-integral of Green's function in Eq. 16 is also performed by the QMC simulation method as before. After averaging this site-dependent Green's function over all the N sites of the system, the photoemission spectral function [$\equiv N_\sigma(\omega)$] can be reproduced through the analytic continuation as,

$$\frac{1}{N}\sum_{l}G_\sigma(l,\tau)=-\int_{-\infty}^{+\infty}\frac{e^{-\tau\omega}}{1+e^{-\beta\omega}}N_\sigma(\omega)d\omega. \tag{17}$$

Finally, after imposing the Fermi-Dirac function $f(\omega)=1/[\exp(\beta\omega)+1]$, the PES intensity is given as $I(\omega)=\sum_\sigma N_\sigma(\omega)f(\omega)$, which can be compared with the experimental data.

3.2. Results and discussions

Since we focus on the spectral region close to the Fermi level, we use a simple cubic lattice of $4\times4\times4$ in real calculation without paying much attention to the detail of carbon valence band. As we just count the e-ph coupling at the doped sites, the phonon effect is not obvious in the whole system PES after averaging over all sites. For this reason, in the following, we will also present the PES of doped sites to illustrate the phonon effect.

Fig. 3 shows the spectra for the simple cubic lattice at light (3.12%) and heavy (12.5%) doping rates, with a weak e-ph coupling of S=0.25 eV. From the whole system PES (full lines), one can clearly see the emergence of a Fermi edge with the increase of doping percentage. In the lightly doped case, the impurity levels are a little above the top of valence band, indicating the system is a semiconductor. While in the heavily doped case, the impurity band expands to overlap the top of valence band and closes the activation gap, leading to a semiconductor-metal phase transition. In the spectra of boron-doped sites (dotted lines), one notices that, in addition to a broad hump due to the so-called Fano effect[9], a satellite structure also appears in each case

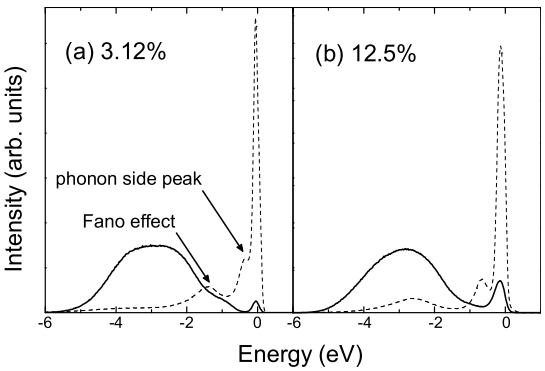

Figure 3. The QMC-calculated spectra for a simple cubic lattice of light (left) and heavy (right) doping rates, at a weak e-ph coupling. Zero is the position of Fermi level. Full lines denote the PES of whole system, and dotted lines the spectra of doped sites.

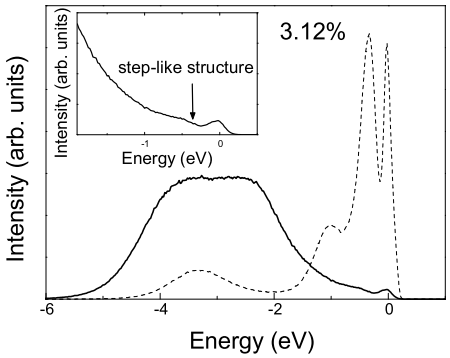

Figure 4. The co-existence of Fermi edge and step-like structure in the PES, at a low doping rate and a strong e-ph coupling, by QMC. Full (dotted) line is the spectrum of whole system (doped sites). The inset zooms in the solid line near the Fermi level.

a little below the Fermi level. We should note this side structure is just the quantum phonon peak due to the e-ph coupling. Meanwhile, because of the Fano effect, this phonon structure is modified by the impurity band to have a shoulder-like shape, rather than a δ-like form as in the localized electron case of Ref. [8].

In Fig. 4, we show the spectra of a system with a strong e-ph coupling of S=0.50 eV, and a low doping rate of 3.12%. Comparing with Fig. 3(a), one clearly finds that, a large e-ph coupling at the doped sites greatly contributes to the expansion of impurity band, so that the Fermi edge is clearly observed in the whole system PES (full line). Moreover, the second phonon side peak also appears due to the multi-phonon processes aroused by the strong e-ph coupling, corresponding to a step-like structure in the whole system PES, as affirmed in the inset.

4. Summary

We develop a new path-integral theory to calculate the PES of correlated many-electron systems. The isotopic shift in the ARPES of Bi2212 is investigated by this theory based on a model including both e-e and off-diagonal quadratic e-ph interactions. Our calculation demonstrates that the band shift is primarily triggered by the e-ph coupling, while the presence of e-e repulsion tends to suppress this effect. We also apply this theory to the MIH model on a doped cubic lattice to clarify the spectral properties of BDD. It is clearly shown in the PES that a semiconductor-metal phase transition takes place due to the increases of e-ph coupling and dopant concentration. Furthermore, the presence of Fermi edge and phonon step-like structure indicates the co-existence of two basic characters of electron, itineracy and localization, in BDD.

References

[1] Gweon G -H, Sasagawa T, Zhou S Y, Graf J, Takagi H, Lee D -H and Lanzara A 2004 *Nature* **430** 187
[2] Douglas J F *et al.* 2007 *Nature* **446** E5
[3] Ekimov E A *et al.*, 2004 *Nature* **428** 542
[4] Tomita N and Nasu K 1997 *Phys. Rev.* B **56** 3779
[5] Ji K, Zheng H and Nasu K 2004 *Phys. Rev.* B **70** 085110
[6] Collins A T and Williams A W S, 1971 *J. Phys.* C **4** 1789
[7] Ishizaka K *et al.*, 2006 *Science and Technology of Advanced Materials* **7** S17-S21
[8] Mahan G D 2000 *Many-Particle Physics* 3rd ed. (New York: Plenum) p 226
[9] Fano U, 1961 *Phys. Rev.* **124** 1866